1

Basic Principles

1.1 Introduction

Spectroscopy is the study of the interaction between matter and electromagnetic radiation. Atoms and molecules have a range of discrete energy levels corresponding to different, quantized electronic, vibrational, or rotational states. The interaction between atoms and electromagnetic radiation is characterized by the absorption and emission of photons with an energy that exactly matches the energy level difference between two states. Since the energy of a photon is proportional to the frequency, the different forms of spectroscopy are often distinguished on the basis of the frequencies involved. For instance, absorption and emission between the electronic states of the outer electrons typically require frequencies in the ultraviolet (UV) range, hence giving rise to UV spectroscopy. Molecular vibrational modes are characterized by frequencies just below visible red light and are thus studied with infrared (IR) spectroscopy. Nuclear magnetic resonance (NMR) spectroscopy uses radiofrequencies, which are typically in the range of 10–1000 MHz.

NMR is the study of the magnetic properties and related energies of nuclei. The absorption of radiofrequency energy can be observed when the nuclei are placed in a (strong) external magnetic field. Purcell et al. [1] at MIT, Cambridge and Bloch et al. [2–4] at Stanford simultaneously, but independently discovered NMR in 1945. In 1952, Bloch and Purcell shared the Nobel Prize in Physics in recognition of their pioneering achievements [5, 6]. At this stage, NMR was purely an experiment for physicists to determine the nuclear magnetic moments of nuclei. NMR could only develop into one of the most versatile forms of spectroscopy after the discovery that nuclei within the same molecule absorb energy at different resonance frequencies. These so-called chemical shift effects, which are directly related to the chemical environment of the nuclei, were first observed in 1949 by Proctor and Yu [7], and independently by Dickinson [8]. The ability of NMR to provide detailed chemical information on compounds was firmly established when Arnold et al. [9] in 1951 published a high-resolution ^{1}H NMR spectrum of ethanol in which separate signals from methyl, methylene, and hydroxyl protons could be clearly recognized.

In the first two decades, NMR spectra were recorded in a continuous wave mode in which the magnetic field strength or the radio frequency was swept through the spectral area of interest, while keeping the other fixed. In 1966, NMR was revolutionized by Ernst and Anderson [10] who introduced pulsed NMR in combination with Fourier transformation. Pulsed or Fourier transform NMR is at the heart of all modern NMR experiments.

The induced energy level difference of nuclei in an external magnetic field is very small when compared to the thermal energy at room temperature, making it that the energy levels

COPYRIGHTED MATERIAL

In Vivo *NMR Spectroscopy: Principles and Techniques*, Third Edition. Robin A. de Graaf.
© 2019 John Wiley & Sons Ltd. Published 2019 by John Wiley & Sons Ltd.

are almost equally populated. As a result the absorption of photons is very low, making NMR a very insensitive technique when compared to the other forms of spectroscopy. However, the low-energy absorption makes NMR also a noninvasive and nondestructive technique, ideally suited for *in vivo* measurements. It is believed that, by observing the water signal from his own finger, Bloch was the first to perform an *in vivo* NMR experiment. Over the following decades, NMR studies were carried out on various biological samples like vegetables and mammalian tissue preparations. Continued interest in defining and explaining the properties of water in biological tissues led to the promising report of Damadian in 1971 [11] that NMR properties (relaxation times) of malignant tumorous tissues significantly differs from normal tissue, suggesting that proton NMR may have diagnostic value. In the early 1970s, the first experiments of NMR spectroscopy on intact living tissues were reported. Moon and Richards [12] used ^{31}P NMR on intact red blood cells and showed how the intracellular pH can be determined from chemical shift differences. In 1974, Hoult et al. [13] reported the first study of ^{31}P NMR to study intact, excised rat hind leg. Acquisition of the first ^{1}H NMR spectra was delayed by almost a decade due to technical difficulties related to spatial localization, and water and lipid suppression. Behar et al. [14] and Bottomley et al. [15] reported the first ^{1}H NMR spectra from rat and human brain, respectively. Since the humble beginnings, *in vivo* MR spectroscopy (MRS) has grown as an important technique to study static and dynamic aspects of metabolism in disease and in health.

In parallel with the onset of *in vivo* MRS, the world of high-resolution, liquid-state NMR was revolutionized by the introduction of 2D NMR by Ernst and coworkers [16] based on the concept proposed by Jeener in 1971 [17]. The development of hundreds of 2D methods in the following decades firmly established NMR as a leading analytical tool in the identification and structure determination of low-molecular weight chemicals. Richard Ernst was awarded the 1991 Nobel Prize in Chemistry for his contributions to the methodological development of NMR [18]. The application of multidimensional NMR to the study of biological macromolecules allowed determination of the 3D structure of proteins in an aqueous environment, providing an alternative to X-ray crystallography. Kurt Wuthrich was awarded the 2002 Nobel Prize in Chemistry for his contributions to the development of protein NMR and 3D protein structure determination [19].

Around the same time reports on *in vivo* MRS appeared, Lauterbur [20] and Mansfield and Grannell [21] described the first reports on a major constituent of modern NMR, namely *in vivo* NMR imaging or magnetic resonance imaging (MRI). By applying position-dependent magnetic fields in addition to the static magnetic field, they were able to reconstruct the spatial distribution of nuclear spins in the form of an image. Lauterbur and Mansfield shared the 2003 Nobel Prize in Medicine [22, 23]. Since its inception, MRI has flourished to become the leading method for structural and functional imaging with methods like diffusion tensor imaging (DTI) and blood oxygenation level-dependent (BOLD) functional MRI.

As a leading clinical and research imaging modality, the theoretical and practical aspects of MRI are covered in a wide range of excellent textbooks [24–26]. While MRS is based on the same fundamental principles as MRI, the practical considerations for high-quality MRS are very different. This book is dedicated to providing a robust description of current *in vivo* MRS methods, with an emphasis on practical challenges and considerations. This chapter covers the principles of NMR that are common to both MRI and MRS. Starting with classical arguments, the concepts of precession, coherence, resonance, excitation, induction, and relaxation are explained. The quantum mechanical view of NMR is briefly reviewed after which the phenomena of chemical shift and scalar coupling will be described, as well as some elementary processing of the NMR signal.

1.2 Classical Magnetic Moments

The discovery of NMR by Bloch and Purcell in 1945 was not a serendipitous event, but was based on the work by Rabi [27, 28] in the previous decade on magnetic resonance of individual particles in a molecular beam for which he received the 1944 Nobel Prize in Physics. While both groups reported the detection of signal associated with proton magnetic moments, the experimental setups as well as the conceptualization of the NMR phenomenon were very different.

Bloch approached NMR from a classical point of view in which the orientation of magnetic moments is gradually changed by an oscillating magnetic field. This would ultimately lead to the detection of NMR signal from water protons through electromagnetic induction in a nearby receiver coil. Purcell viewed the NMR phenomenon based on quantum mechanics, in close analogy to other spectroscopic methods in which transitions are induced between energy levels by quanta of energy provided by radiofrequency (RF) waves. Purcell described the absorption of energy provided by an oscillating RF field by the protons in solid paraffin. A wonderful overview of the two discoveries of NMR is given by Rigden [29] and Becker et al. [30] as well as by the Nobel lectures of Bloch [5] and Purcell [6].

The spectroscopic or quantum mechanical view often takes center stage in the introduction of many text books, including the previous editions of this book. The main reason for this approach is that a full quantum mechanical description of NMR can account for all observed phenomena, including those that have no classical analog, like scalar or J-coupling. However, as the quantum description of NMR does not deal directly with observable magnetization, but rather with the energetic state of the system, it does not provide an intuitive, physical picture. In the classical view of NMR, the magnetic moments of the individual nuclear spins are summed up to form a macroscopic magnetization vector that can be followed over time using classical electromagnetism concepts. This provides a familiar picture that can be used to follow the fate of magnetization under a wide range of experimental conditions. The classical picture is advocated here, starting with a magnetized needle as found in a compass.

As with all magnets, the compass needle is characterized by a magnetic north and south pole from which the magnetic field lines exit and enter the needle, respectively (Figure 1.1A). The magnetic field lines shown in Figure 1.1A can be summarized by a magnetic moment, μ, describing both the amplitude and direction. In the absence of an external magnetic field the compass needle has no preference in spatial orientation and can therefore point in any direction.

When placed in an external magnetic field, such as the Earth's magnetic field, the compass needle experiences a torque (or rotational force) that rotates the magnetic moment towards a parallel orientation with the external field (Figure 1.1B). As the magnetic moment "overshoots" the parallel orientation, the torque is reversed and the needle will settle into an oscillation or frequency that depends on the strengths of the external magnetic field and the magnetic moment. Due to friction between the needle and the mounting point, the amplitude of the oscillation is dampened and will ultimately result in the stabile, parallel orientation of the needle with respect to the external field (Figure 1.1C) representing the lowest magnetic energy state (the antiparallel orientation represents the highest magnetic energy state).

The equilibrium situation (Figure 1.1C) can, besides mechanical means, be perturbed by additional magnetic fields as shown in Figure 1.1D. When a bar magnet is moved towards the compass, the needle experiences a torque and is pushed away from the parallel orientation. When the bar magnet is removed, the needle oscillates as shown in Figure 1.1B before returning to the equilibrium situation (Figure 1.1C). However, if the bar magnet is moved back and

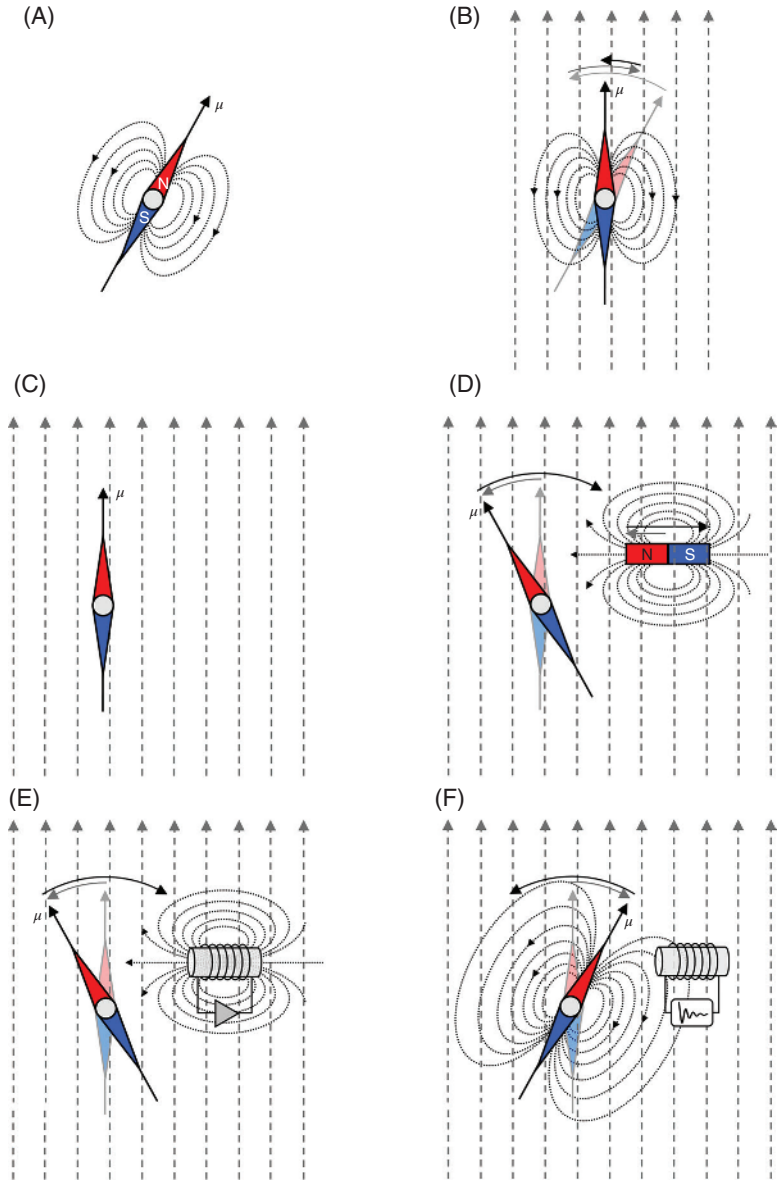

Figure 1.1 Oscillations of a classical compass needle. (A) A compass needle with a magnetic north and south pole creates a dipolar magnetic field distribution of which the amplitude and direction are characterized by the magnetic moment μ. (B) When placed in an external magnetic field the magnetic moment oscillates a number of times before (C) settling in a parallel orientation with the external magnetic field. Note that in Earth's magnetic field the compass needle points to the magnetic south, which happens to be close to geographical north. (D) The needle can be perturbed with a bar magnet, whereby the perturbation reaches maximum effect when the bar movement matches the natural frequency of the needle. (E) The bar magnet can be replaced by an alternating current in a coil. (F) The same coil can also be used to detect the oscillating magnetic moment of the needle through electromagnetic induction.

forth relative to the compass, the needle can be made to oscillate continuously. When the movement frequency of the bar magnet is very different from the natural frequency of the needle (Figure 1.1B), the effect of the bar magnet is not constructive and the needle never deviates far from the parallel orientation. However, when the frequency of the bar magnet

movement matches the natural frequency of the needle, the repeated push from the bar magnet on the needle is constructive and the needle will deviate increasingly further from the parallel orientation. When the bar magnet has a maximum effect on the needle, the system is in resonance and the oscillation is referred to as the resonance frequency. A similar situation arises when pushing a child in a swing; only when the child is pushed in synchrony with the natural or resonance frequency of the swing set does the amplitude get larger.

The bar magnet can be replaced with an alternating current in a copper coil as shown in Figure 1.1E. The alternating current generates a time-varying magnetic field that can perturb the compass needle. When the frequency of the alternating current matches the natural frequency of the needle, the system is in resonance and large deviations of the needle can be observed with modest, but constructive "pushes" from the magnetic field produced by the coil.

The compass needle continues to oscillate at the natural frequency for some time following the termination of the alternating current (Figure 1.1F). The compass needle creates a time-varying magnetic field that can be detected through Faraday electromagnetic induction in the same coil previously used to perturb the needle. The induced voltage, referred to as the Free Induction Decay (FID), will oscillate at the natural frequency and will gradually reduce in amplitude as the compass needle settles into the parallel orientation.

Figure 1.1 shows that the MR part of NMR can be completely described by classical means. It is therefore also not surprising that Bloch titled his seminal paper "Nuclear induction" [2, 4] as the electromagnetic induction is an essential part of MR detection. The magnetic effects summarized in Figure 1.1 are readily reproduced "on the bench" and provide an excellent means of experimentally demonstrating some of the concepts of MR [31].

1.3 Nuclear Magnetization

Any rotating object is characterized by angular momentum, describing the tendency of the object to continue spinning. Subatomic particles like electrons, neutrons, and protons have an *intrinsic* angular moment, or spin that is there even though the particle is not actually spinning. Electron spin results from relativistic quantum mechanics as described by Dirac in 1928 [32] and has no classical analog. For the purpose of this book the existence of spin is simply taken as a feature of nature. Particles with spin always have an intrinsic magnetic moment. This can be conceptualized as a magnetic field generated by rotating currents within the spinning particle. This should, however, not be taken too literal as the particle is not actually rotating. Note that in the NMR literature, spin and magnetic moments are used interchangeably.

Protons are abundantly present in most tissues in the form of water or lipids. In the human brain, a small cubic volume of $1 \times 1 \times 1$ mm contains about 6×10^{19} proton spins (Figure 1.2A and B). In the absence of an external magnetic field, the spin orientation has no preference and the spins are randomly oriented throughout the sample (Figure 1.2B). For a large number of spins this can also be visualized by a "spin-orientation sphere" (Figure 1.2C) in which each spin has been placed in the center of a Cartesian grid. Summation over all orientations leads to a (near) perfect cancelation of the magnetic moments and hence to the absence of a macroscopic magnetization vector. It should be noted that the concept of a spin-orientation sphere has been used throughout the NMR literature [33–35], albeit sporadically. The description of the NMR phenomenon based on a spin-orientation sphere will be advocated here as a classical, intuitive alternative to the quantum-mechanical view.

Up to this point the nuclear magnetic moments behave similarly to the magnetic moments associated with classical compass needles. However, unlike compass needles nuclear magnetic moments have intrinsic angular momentum or spin which can be visualized as a nucleus spinning around its own axis (Figure 1.2D). When a nuclear spin is placed in an external

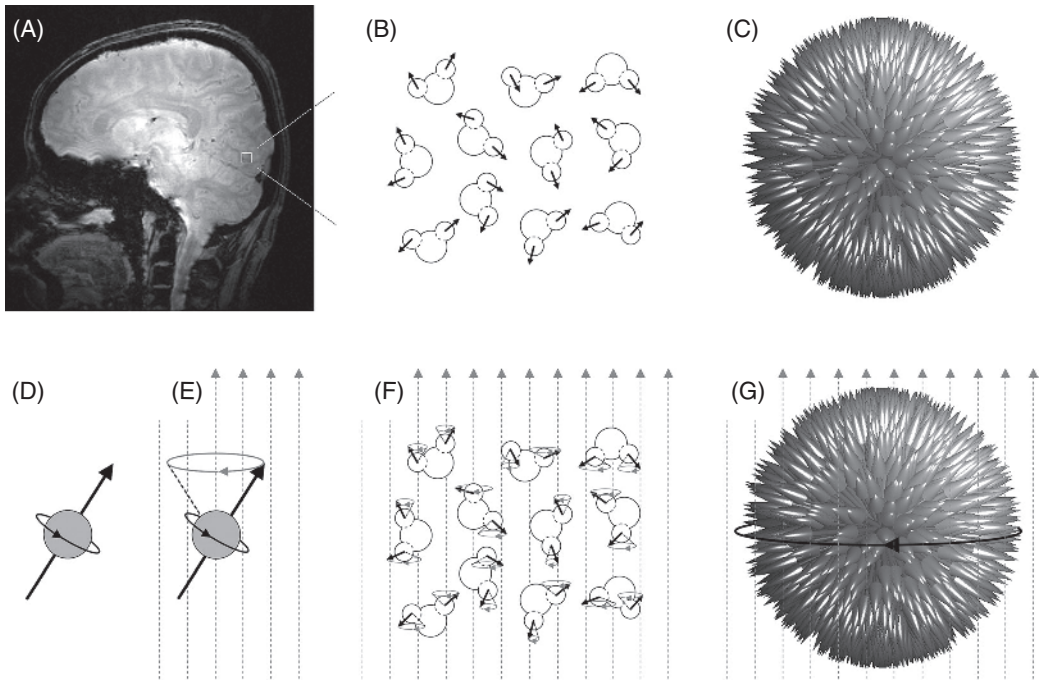

Figure 1.2 Precession of nuclear spins. (A, B) A small 1 μl volume from the human brain contains about 6×10^{19} protons, primarily located in water molecules. (B, C) In the absence of a magnetic field the proton spins have no orientational preference, leading to a randomly distributed "spin-orientation sphere." (D) Unlike compass needles, nuclear magnetic moments have intrinsic angular momentum or spin that leads to (E) a precessional motion when placed in a magnetic field. (F) All spins attain Larmor precession, but retain their random orientation to a good first approximation. (G) While the spin-orientation sphere also remains random when placed in a magnetic field, the entire sphere will attain Larmor precession.

magnetic field (Figure 1.2E) the presence of angular momentum makes the magnetic moment precess around the external magnetic field (Figure 1.2E). This effect is referred to as Larmor precession and the corresponding Larmor frequency ν_0 (in MHz) is given by

$$\nu_0 = \frac{\omega_0}{2\pi} = \frac{\gamma}{2\pi} B_0 \tag{1.1}$$

where γ is the gyromagnetic (or magnetogyric) ratio (in rad·MHz T^{-1}) and B_0 is the magnetic field strength (in T). The gyromagnetic ratio, which is constant for a given nucleus, is tabulated in Table 1.1. For protons at 7.0 T the Larmor frequency is 298 MHz. It should be noted that Larmor precession occurs for any spinning magnetic moment in a magnetic field, including classical objects and that it was described decades before the discovery of NMR [36].

When the protons depicted in Figure 1.2B are subjected to an external magnetic field, every spin starts to precess around the magnetic field with the same Larmor frequency. The Larmor frequency is independent of the angle between the external magnetic field and an individual spin. As the orientation of the magnetic moment with respect to the main magnetic field does (initially) not change, the spin-orientation sphere representation of Figure 1.2C remains unchanged with the exception that the entire sphere is rotating around the magnetic field at the Larmor frequency. If Larmor precession would be the only effect induced by the external magnetic field, then NMR would never have developed into the versatile technique as we know it today.

Table 1.1 NMR properties of biologically relevant nuclei encountered in *in vivo* NMR.

Isotope	Spin	Gyromagnetic ratio (rad·MHz T^{-1})	NMR frequency ratio (% of ^{1}H)	Natural abundance (%)
^{1}H	1/2	267.522	100.000	99.985
^{2}H	1	41.066	15.351	0.015
^{3}He	1/2	−203.802	76.179	0.000 14
^{7}Li	3/2	103.977	38.864	92.58
^{13}C	1/2	67.283	25.145	1.108
^{14}N	1	19.338	7.226	99.630
^{15}N	1/2	−27.126	10.137	0.370
^{17}O	5/2	−36.281	13.556	0.037
^{19}F	1/2	251.815	94.094	100.000
^{23}Na	3/2	70.808	26.452	100.000
^{29}Si	1/2	−53.190	19.867	4.7
^{31}P	1/2	108.394	40.481	100.000
^{33}S	3/2	20.557	7.676	0.76
^{35}CI	3/2	26.242	9.798	75.53
^{37}CI	3/2	21.844	8.156	24.47
^{39}K	3/2	12.501	4.667	93.100
^{129}Xe	1/2	−74.521	27.810	26.44

Fortunately, there is a second, more subtle effect that ultimately leads to a net, macroscopic magnetization vector that can be detected. The water molecules in Figure 1.2B are in the liquid state and therefore undergo molecular tumbling with a range of rotations, translations, and collisions. As a result, the amplitude and orientation of the magnetic field generated by one proton at the position of another proton changes over time (Figure 1.3A). When the local field fluctuation matches the Larmor frequency, it can perturb the spin orientation. These perturbations are largely, but not completely, random. The presence of a strong external magnetic field slightly favors the parallel spin orientation. As a result, over time the completely random spin orientation distribution (Figure 1.3B) changes into a distribution that is slightly biased towards a parallel spin orientation (Figure 1.3C). Visually, the spin distributions in the absence (Figure 1.3B) and presence (Figure 1.3C) of an external magnetic field look similar because the net number of spins that are biased towards the parallel orientation is very small, on the order of one in a million. The situation becomes visually clearer when the spin distribution is separated into spins that have a random orientation distribution (Figure 1.3D) and spins that are slightly biased towards a parallel orientation (Figure 1.3E). Adding the magnetic moments of Figure 1.3D does not lead to macroscopic magnetization similar to the situation in Figure 1.2G. However, adding the magnetic moments of Figure 1.3E leads to a macroscopic magnetization vector parallel to the external magnetic field. As the external magnetic field only biases the spin distribution along its direction, the spin distribution in the two orthogonal, transverse directions is still random.

The microscopic processes detailed in Figure 1.3A–E can be summarized at a macroscopic level as shown in Figure 1.3F. In the absence of a magnetic field ($t < 0$) the sample does not produce macroscopic magnetization. When an external magnetic field is instantaneously turned on ($t = 0$), the macroscopic magnetization exponentially grows over time where it plateaus at

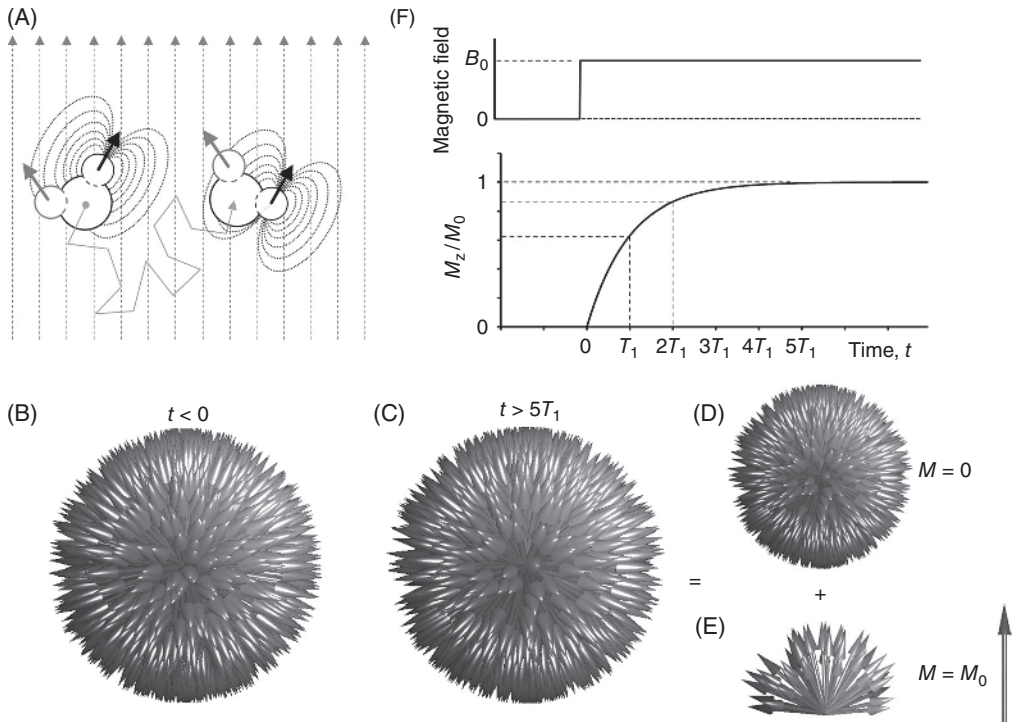

Figure 1.3 Appearance of macroscopic magnetization through T_1 relaxation. (A) Molecular tumbling and Brownian motion causes spin 1 (gray) to experience a wide range of magnetic field fluctuations originating from spin 2 (black) and other spins outside the water molecule. Magnetic field fluctuations of the proper frequency can change the spin orientation. While the perturbations are largely random, there is a very slight bias towards a parallel orientation with the external magnetic field. Over time the almost random perturbations transform a completely random spin-orientation sphere (B) into one that has a small polarization M_0 (C). The small polarization M_0 can be visualized better when the spins with a random orientation (D) are separated from the spins that have attained a slight bias (E). (F) Macroscopically the small polarization M_0 appears exponentially over time with a characteristic T_1 relaxation time constant according to Eq. (1.2).

a value corresponding to the thermal equilibrium magnetization, M_0. The appearance of macroscopic magnetization can be described by

$$M_z(t) = M_0 - \left(M_0 - M_z(0)\right)e^{-t/T_1} \tag{1.2}$$

where T_1 is the longitudinal relaxation time constant and $M_z(0)$ is the longitudinal magnetization at time zero. In the case of Figure 1.3, the initial longitudinal magnetization is zero, i.e. $M_z(0) = 0$. At the time of the first NMR studies, little was known about T_1 relaxation times in bulk matter. Both originators of NMR, Bloch and Purcell, were acutely aware that a very long T_1 relaxation time constant could seriously complicate the detection of nuclear magnetism. As a precaution, Purcell used an exceedingly small RF field such as not to saturate the sample [1], whereas it is rumored that Bloch left his sample in the magnet to reach thermal equilibrium while on a skiing trip [29]. Following the initial experiments it became clear that T_1 relaxation time constants can range from milliseconds to minutes, with water establishing thermal equilibrium in seconds. Extraordinarily long T_1 relaxation times may, however, have been the main reason for earlier, negative reports by Gorter [37, 38] on the detection of NMR in bulk matter.

The longitudinal magnetization vector represents the signal that will be detected in an NMR experiment. However, the static, longitudinal magnetization is never detected directly as its

small contribution would be overwhelmed by much larger contributions from magnetization associated with electron currents within atoms and molecules. Instead, the longitudinal magnetization is brought into the transverse plane where the precessing magnetization can induce signal in a receiver coil at the very specific Larmor frequency.

The size of the longitudinal equilibrium magnetization and thereby the strength of the induced NMR signal is proportional to the number of spins that are biased towards a parallel orientation with the main magnetic field. The distribution of spin orientations and hence the bias in it can be calculated through the Boltzmann distribution which provides the probability P that a spin is in a certain orientation with an associated energy E according to

$$P(E) \propto e^{-E/kT} \tag{1.3}$$

where k is the Boltzmann constant (1.38066×10^{-23} J K^{-1}) and T is the absolute temperature in Kelvin. Equation (1.3) expresses the chance P of finding a particle with energy E in that state rather than in a random state determined by the available thermal energy of the environment (kT). For nuclear spins the energy limits are $\pm\mu B$, where μ is the magnetic moment and B is the external magnetic field. The lower and higher energies correspond to nuclear spins parallel and antiparallel to the external magnetic field, respectively. Using either a continuous distribution of spin orientations as shown in Figure 1.3C or a quantized distribution (see Section 1.11) the longitudinal equilibrium magnetization can be calculated from the Boltzmann distribution and is given by

$$M_0 = \frac{N\gamma^2 h^2 B_0}{16\pi^2 kT} \tag{1.4}$$

Equation (1.4) reveals several important features of the signals detected by NMR. Firstly, the thermal equilibrium magnetization M_0 is directly proportional to the number of spins N in the sample. This feature makes NMR a quantitative method in which the detected signals are, in principle, proportional to the concentration. The quadratic dependence of M_0 on the gyromagnetic ratio γ implies that nuclei resonating at high frequency (see Eq. (1.1)) generate the strongest NMR signals. Hydrogen has the highest γ of the commonly encountered nuclei, and has therefore the highest relative sensitivity. The linear dependence of M_0 on the magnetic field strength B_0 implies that higher magnetic fields improve the sensitivity. In fact this argument (and the related increase in chemical shift dispersion) has caused a steady drive towards higher magnetic field strength which now typically range from 1.5 T to circa 24 T (or up to circa 11.7 T for human applications). Finally, the inverse proportionality of M_0 to the temperature T indicates that sensitivity can be enhanced at lower sample temperatures. While the latter option is unrealistic for direct *in vivo* applications, it is being utilized to increase M_0 by orders of magnitude in hyperpolarized MR (see Chapter 3). The actual experimental sensitivity is determined by many additional factors, like RF coil characteristics, pulse sequence details, sample volume, natural abundance of the nucleus studied, sample noise, relaxation parameters, and spectral resolution. Although some factors can be predicted by Eq. (1.4), others need a more detailed treatment and can be found throughout the book.

1.4 Nuclear Induction

The orientation of a compass needle in Figure 1.1 could be changed with an additional magnetic field perpendicular to the magnetic moment. Similarly, a second magnetic field, B_1, is used to change the orientation of the longitudinal magnetization, M_0. Figure 1.4A shows the spin-orientation sphere at thermal equilibrium as being composed of randomly oriented

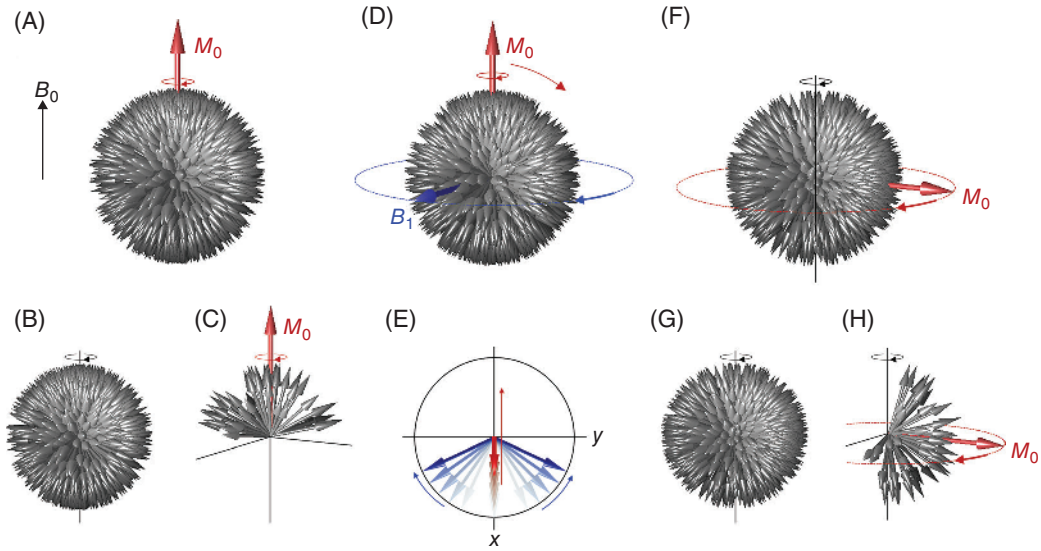

Figure 1.4 Excitation of nuclear spins. (A) A collection of nuclear spins give rise to macroscopic magnetization (red vector) parallel to B_0 at thermal equilibrium. (B) The nuclear spin orientations are largely random, with (C) only a minor amount contributing to the macroscopic magnetization. (D) A secondary magnetic field, B_1, perpendicular to B_0 and oscillating at the Larmor frequency has a constant phase relation with the spin magnetic moments. As a result, the B_1 magnetic field applies a constant torque during each Larmor revolution, leading to a rotation of the entire spin-orientation sphere. (E) The rotating B_1 field shown in (D) is typically achieved by a co-sinusoidally varying magnetic field (red arrow) which is equivalent to the sum of clockwise and anticlockwise vectors (blue arrows). Whereas the clockwise component achieves excitation as shown in (D), the anticlockwise component can for most practical purposes be ignored. (F–H) When the length and amplitude of the B_1 magnetic field is adjusted to provide a 90° rotation, the RF pulse has achieved excitation of the nuclear spins. Note that the entire spin-orientation sphere has been rotated by 90°, whereby (G) the randomly-oriented spins are still random and (H) the biased spins now provide a macroscopic magnetization vector in the transverse plane.

spins (Figure 1.4B) and a small number of spins with a net bias towards a parallel orientation (Figure 1.4C). Each of the spins undergoes Larmor precession around the magnetic field on its own cone, dictated by the initial orientation of the magnetic moment. When a stationary magnetic field B_1 is applied, the spins would not be perturbed in any significant manner since any rotation achieved during the first half of a Larmor precession cycle $1/(2\nu_0)$ (=1.68 ns for ^{1}H at 7 T) would be undone during the second half. In other words, a stationary magnetic field B_1 is not in resonance with the spins and its effect is therefore negligible. However, as shown for the compass needle in Figure 1.1, the second magnetic field can have a large effect when its frequency matches the natural frequency of the compass needle. Figure 1.4D shows the same spin-orientation sphere in the presence of a rotating magnetic field B_1 whose frequency equals the Larmor frequency. Since the angle between the magnetic moments and the magnetic field B_1 is constant, the entire spin-orientation sphere and hence the net macroscopic magnetization experiences a coherent rotation towards the transverse plane. When the amplitude and duration of the B_1 field is adjusted as to achieve a 90° rotation of the magnetization from the longitudinal axis into transverse plane (Figure 1.4F–H), the spins have undergone an excitation and the B_1 field is referred to as an excitation pulse. When the amplitude or duration of the B_1 field is doubled, the initial thermal equilibrium magnetization

undergoes a 180° rotation, referred to as an inversion which is achieved by an inversion pulse. Following excitation, the B_1 field is removed leaving the magnetization in the transverse plane to be detected through electromagnetic induction in a nearby receiver coil. It should be noted that the magnitude of the rotating B_1 magnetic field is typically five to six orders of magnitude smaller than the static B_0 magnetic field. In addition, it should be realized that NMR uses *magnetic* fields rotating at the RF frequency, not electromagnetic RF waves [39, 40]. The electric component of electromagnetic RF waves is not relevant for NMR signal excitation or detection and proper RF coil design is aimed at minimizing its contribution. Unfortunately, electric fields cannot be eliminated entirely and are responsible for RF-induced sample heating (see Chapter 10).

At this point it should be mentioned that the secondary magnetic field B_1 is typically not applied as a rotating magnetic field, but rather as a cosine-modulated magnetic field traversing between the $+x$ and $-x$ axes (Figure 1.4E). However, a linear cosine-modulated magnetic field can be seen as the vector sum between clockwise and counterclockwise rotating components (Figure 1.4E). The counterclockwise component influences the spins to the order $(B_1/2B_0)^2$ and is known as the Bloch–Siegert shift [41]. Under most experimental conditions the counterclockwise rotating component can be ignored as it is not in resonance with the spins, leaving just the clockwise-rotating component to act on the nuclear magnetic moments.

1.5 Rotating Frame of Reference

The rotation of the magnetization vector during an RF pulse is fairly complex in a standard nonrotating frame-of-reference *xyz*, also known as the laboratory frame. In the laboratory frame the magnetization follows a complex path (Figure 1.5A) rotating around B_0 at the Larmor frequency while simultaneously also rotating around the secondary magnetic field B_1. For most applications, the Larmor precession is a constant motion that complicates visualization of rotations induced by the RF pulse. The Larmor precession can be visually removed by switching from a nonrotating laboratory frame to a frame-of-reference $x'y'z'$ that is rotating at the RF pulse frequency (Figure 1.5B). In the rotating frame the B_1 magnetic field is always along the x' axis, whereas the magnetization rotates in the $y'z'$ plane. With the observer still in the stationary laboratory frame, the motion of the magnetization is still as complicated as in Figure 1.5B. However, when the observer is placed within the rotating $x'y'z'$ frame, the observer also rotates at the RF pulse frequency making the associated motion invisible. The only motion that remains in the rotating frame $x'y'z'$ is the simple rotation of the magnetization around the B_1 magnetic field from the z' axis towards the $x'y'$ plane (Figure 1.5C). As is the case for the majority of NMR literature, all subsequent discussions will take place in the rotating frame of reference. Switching from a laboratory frame *xyz* to a rotating frame $x'y'z'$ is mathematically equivalent to reducing the very large B_0 (in T) or $(\gamma/2\pi)B_0$ (in Hz) magnetic field vector along the z/z' axis to zero. When the RF pulse and Larmor frequencies are equal, the RF pulse is said to be on-resonance and the $(\gamma/2\pi)B_0$ vector is effectively absent in the rotating frame $x'y'z'$. Any transverse magnetization will not show precession, but appears static along a fixed axis. However, when the RF pulse frequency ν is not equal to the Larmor frequency ν_0, the RF pulse is said to be off-resonance by $\Delta\nu = \nu_0 - \nu$ Hz. In that case a small $\Delta\nu$ vector appears along the z' axis of the rotating frame and any transverse magnetization will rotate around the z' axis at a frequency $\Delta\nu$ (Figure 1.5D). A quantitative treatment of rotating frames can be found in Section 1.7 during description of the Bloch equations.

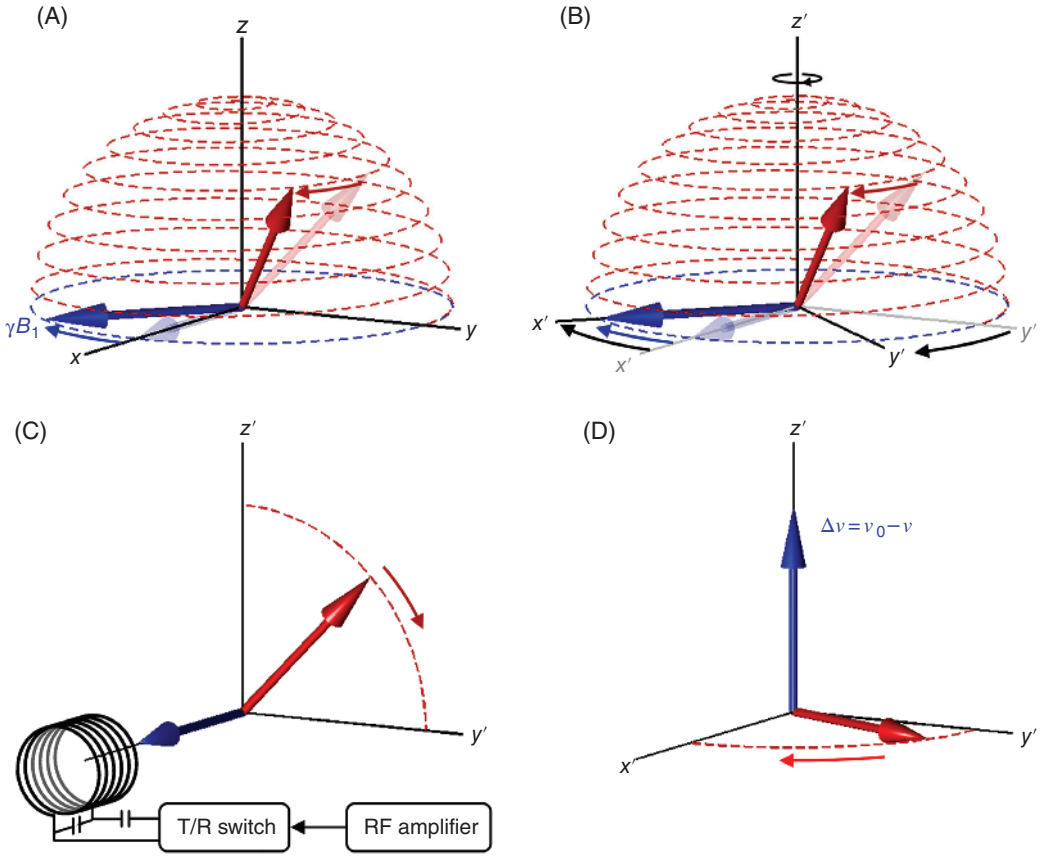

Figure 1.5 Laboratory and rotating frames of references. (A) Rotations of the macroscopic magnetization vector (red) in the nonrotating laboratory frame *xyz*. The magnetization precesses under the influence of the main magnetic field B_0 along the *z* axis and the oscillating magnetic field B_1 in the *xy* plane. Note that the relative oscillations are not drawn to scale. During the time over which the B_1 magnetic field rotates the spins by circa 45°, the spins precess millions of revolutions around the B_0 magnetic field. (B) In a rotating frame $x'y'z'$ that rotates at the RF frequency, the B_1 magnetic field is always aligned along the x' axis. As a nonrotating observer in the laboratory frame, the oscillations of the magnetization have not changed. (C) However, as a rotating observer in the rotating frame, the rotations around the B_0 magnetic field are no longer visible, leaving only the simple rotation of the magnetization around the B_1 magnetic field. For an RF pulse of amplitude B_1 (in T) and duration T (in s), the nutation or flip angle θ (in rad) of the magnetization is given by $\theta = \gamma B_1 T$. RF pulses with nutation angles of 90° and 180° are typically referred to as excitation and inversion pulses. The power for an RF pulse is generated by an RF amplifier and is, via a transmit/receive (T/R) switch and an RF coil, delivered to the sample. Details on RF coils and related hardware can be found in Chapter 10. (D) On-resonance spins, for which the RF pulse frequency ν equals the Larmor frequency ν_0, remain along the y' axis following excitation since the effective magnetic field along the z' axis has been reduced to zero. Off-resonance spins, for which $\nu \neq \nu_0$, experience a small residual magnetic field along the z' axis of $(2\pi\Delta\nu/\gamma)$ which leads to precession at an effective off-resonance frequency $\Delta\nu$. The fate of off-resonance spins *during* an RF pulse is discussed in Chapter 5.

1.6 Transverse T_2 and T_2^* Relaxation

Figure 1.6B shows the situation right after excitation of the longitudinal magnetization into the transverse plane. The spins with a slight bias towards a parallel orientation with the magnetic field before the RF pulse now display a bias towards the y' axis. Addition of all individual magnetic moments leads to a macroscopic magnetization vector along the y' axis (Figure 1.6B,

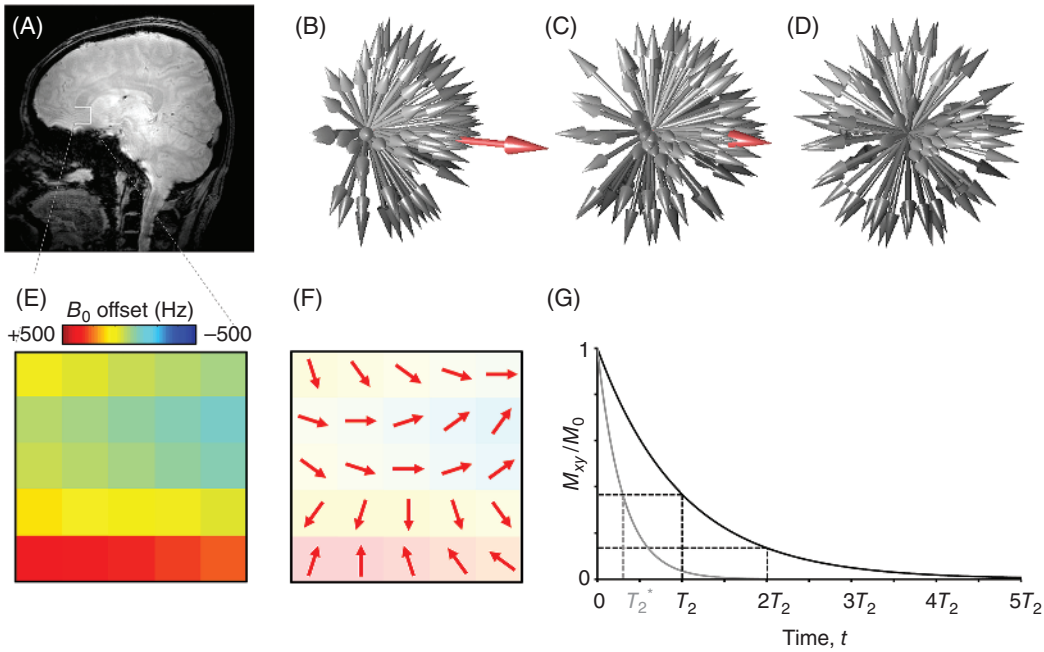

Figure 1.6 Disappearance of macroscopic magnetization through T_2 and T_2^* relaxation. (A) Sagittal MR image through the human head. (B) Collection of nuclear spins that give rise to macroscopic transverse magnetization (red vector) immediately following excitation. (C) Over time random molecular tumblings, similar to those depicted in Figure 1.3A, lead to a gradual loss in phase coherence. (D) After a sufficient amount of time has passed, all phase coherence has been lost and no macroscopic signal can be observed. The irreversible loss of phase coherence due to random molecular processes is an exponential process characterized by a T_2 relaxation time constant (G, black line). Under many circumstances the loss of detectable signal is much faster than that governed by T_2 relaxation and is often due to local magnetic field inhomogeneity. (E) Magnetic field B_0 map from a small part of the human brain depicted in (A). Variation of up to a few ppm in the magnetic field B_0 across the small, but macroscopic volume elements leads to a range of Larmor frequencies according to Eq. (1.1). (F) After some time following excitation, spins with different Larmor frequencies will have attained different phases. As the detected signal originates from all volume elements combined, a variation in phase leads to phase cancelation and thus signal loss. The loss of phase coherence due to magnetic field inhomogeneity in addition to T_2 relaxation is typically described as an exponential process with a T_2^* relaxation time constant (G, gray line). Since the T_2^* relaxation contains contributions from magnetic field inhomogeneity and T_2 relaxation, it can be stated that the T_2^* relaxation time constant is always smaller or equal to the T_2 relaxation time constant. The effects of magnetic field inhomogeneity can be completely removed for a single time point following excitation with a spin-echo pulse sequence (see Chapter 3). The effects of macroscopic magnetic field inhomogeneity can be reduced through shimming, as will be discussed in Chapter 10.

red). Note that the vectors are on-resonance and shown in the rotating frame $x'y'z'$ so that the macroscopic magnetization as well as the individual spins do not display Larmor precession. The situation in Figure 1.6B is a nonequilibrium condition and the spins want to return to thermal equilibrium where a longitudinal magnetization vector exists without any macroscopic transverse component. The reappearance of the longitudinal magnetization is governed by T_1 relaxation and at a time $>5T_1$ the thermal equilibrium magnetization will have been reestablished (see also Figure 1.3). The disappearance of macroscopic transverse magnetization is governed by T_2 relaxation. Right after excitation (Figure 1.6B) the individual spins precess with the same Larmor frequency. However, molecular tumbling and Brownian motion lead to random local field fluctuations as shown in Figure 1.3, such that the Larmor frequencies of different spins start to run out of sync over time (Figure 1.6C). As a result, the total sum of all

magnetic moments is reduced leading to a smaller, macroscopic transverse magnetization vector. After a sufficient amount of time has passed, the Larmor frequencies are completely out of sync leading to the disappearance of macroscopic transverse magnetization. The ability to attain phase coherence in MR is remarkable; for many compounds the spins can undergo millions of Larmor revolutions before any noticeable loss of phase coherence can be detected. The long lifetime of transverse magnetization is one of the most important features of NMR and has allowed the development of a rich variety of pulse sequences interspersing RF pulses with delays. The disappearance of macroscopic magnetization from the transverse plane can be described by

$$M_{xy}(t) = M_{xy}(0)\mathrm{e}^{-t/T_2} \tag{1.5}$$

where T_2 is the transverse relaxation time constant. For ^{1}H NMR in biological tissues the T_2 relaxation time constants (10–300 ms) are typically much shorter than the T_1 relaxation time constants (500–3000 ms). Chapter 3 will discuss T_1 and T_2 relaxation in greater detail. From Figures 1.4 and 1.6 it is clear that the presence of detectable, macroscopic magnetization in the transverse plane relies on phase coherence among the spins that were biased along the z' axis before excitation. As a result, macroscopic transverse magnetization is sometimes referred to as coherence. As will be seen in later chapters, coherence is a broader term that also describes unobservable and correlated transverse magnetization among scalar-coupled spins.

For most MR applications the signal decay observed during the recording of an FID is much faster than governed by T_2 relaxation according to Eq. (1.5). This is due to macroscopic magnetic field inhomogeneity and is illustrated in Figure 1.6E and F. As will be discussed in Chapter 10, differences in magnetic susceptibility between water and air leads to magnetic field inhomogeneity in the proximity to their boundary. A prime example is the transition between air in the nasal cavities and water in the brain, leading to an inhomogeneous magnetic field in the frontal cortex. Figure 1.6E shows a magnetic field map from a small section of the human frontal cortex (Figure 1.6A). While the magnetic field at each location is about 4 T, or 170 MHz, there is a small variation of circa 500 Hz across the spatial locations. When the transverse magnetization is initially formed following excitation, the signal at each location is along the y' axis of the rotating frame. After time t, the spins at position r that are off-resonance by an amount $\Delta\nu = (\gamma/2\pi)\Delta B$ acquire a phase difference given by

$$\Delta\phi(r,t) = 2\pi\Delta\nu(r)t \tag{1.6}$$

leading to the situation in Figure 1.6F where the transverse magnetization in different subvolumes has acquired various amounts of phase. Summation over the entire macroscopic volume will lead to phase cancelation and thus a smaller macroscopic magnetization vector. The process can be written as the combination of Eqs. (1.5) and (1.6) according to

$$M_{xy}(t) = M_{xy}(0)\mathrm{e}^{-t/T_2}\int_r \mathrm{e}^{i\Delta\phi(r,t)}\mathrm{d}r = M_{xy}(0)\mathrm{e}^{-t/T_2^*} \tag{1.7}$$

assuming spatially homogeneous M_{xy} and T_2 relaxation distributions. It follows that in the presence of magnetic field inhomogeneity the disappearance of transverse magnetization is governed by T_2^* relaxation. While T_2^* relaxation is often modeled as an exponential function, the signal decay is governed by the complex integral in Eq. (1.7) which can take on a wide range of (non-exponential) shapes. Whereas both T_2 and T_2^* relaxation are caused by magnetic field

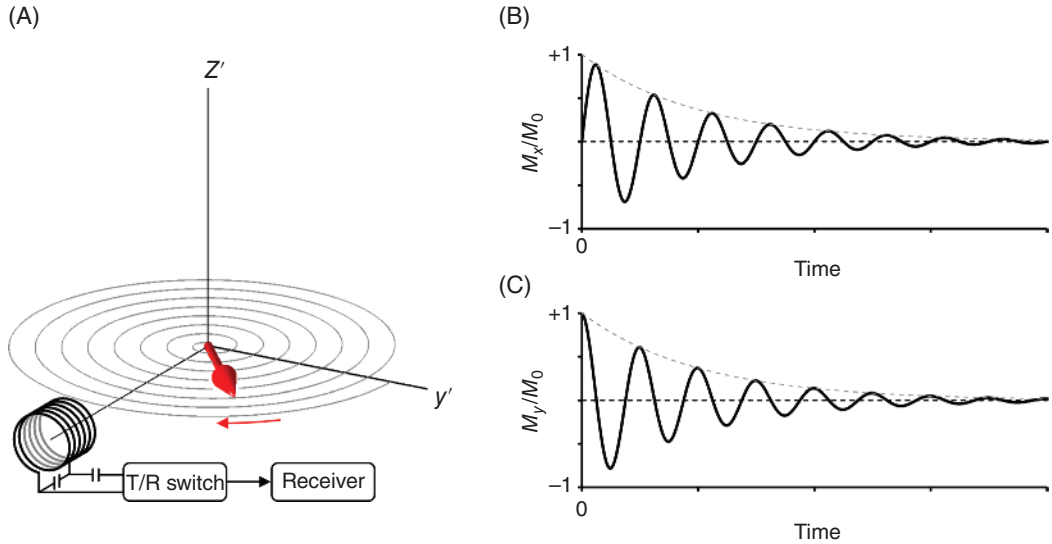

Figure 1.7 Nuclear induction. (A) A rotating, macroscopic magnetization vector induces a voltage in a nearby receive RF coil through electromagnetic induction. Note that the same RF coil that was used to transmit the RF pulse (Figure 1.5C) can be used to receive the FID. The transmit/receive (T/R) switch ensures that the small NMR signal enters the receive chain during reception, while preventing high-powered RF pulses to damage the receive chain during transmission. (B, C) The FID signal is typically sampled along a single axis (x' in (A), giving rise to M_x in (B)) after which the second, orthogonal component is created during the phase-sensitive, quadrature detection step (see Chapter 10).

inhomogeneity leading to a decrease in phase coherence and an overall signal loss, there is an important difference. T_2 relaxation is caused by the inherently random process of fluctuating magnetic fields among the individual spins leading to irreversible signal loss. The additional dephasing associated with T_2^* relaxation is caused by static magnetic field inhomogeneity. Since the cause of the additional dephasing is constant over time, its effects can be reversed with a spin-echo sequence as will be discussed in Chapter 3. In addition, improvements in the magnetic field homogeneity obtained through shimming (Chapter 10) directly lead to longer T_2^* relaxation times and a smaller difference between T_2 and T_2^*.

The rotating, transverse magnetization (Figure 1.7A) gives rise to the NMR FID signal through electromagnetic induction into a nearby receiver coil. Often the same RF coil that was used for RF transmission (or B_1 magnetic field generation, Figure 1.5C) is also used for NMR signal reception (Figure 1.7A). The transmit/receive (T/R) switch ensures that the sensitive receiver electronics are protected when the high-powered RF pulses are transmitted. More details on RF transmit and receive chain elements can be found in Chapter 10. The x and y components of the FID are shown in Figure 1.7B and C. The signal in Figure 1.7 presents the fundamental NMR signal that, despite the extensive discussions up to this point, can be generated with only three elements. Firstly, a strong external magnetic field is required to create the net thermal equilibrium magnetization. Secondly, a time-varying magnetic field rotates the magnetization into the transverse plane where, lastly the precessing magnetization induces the FID signal in a receiver coil. In the following paragraphs and chapters the information content of the FID signal is greatly enhanced through detection of chemical shifts and scalar couplings and through spatial encoding. However, all NMR experiments are fundamentally based on the three operations described in Figures 1.3, 1.4, and 1.7.

1.7 Bloch Equations

Felix Bloch described the motion of the macroscopic magnetization by three phenomenological differential equations that are commonly referred to as the Bloch equations [4]. In the absence of relaxation the rotations of the macroscopic magnetization vector $\boldsymbol{M} = (M_x, M_y, M_z)$ in the laboratory frame is described by

$$\frac{\mathrm{d}M(t)}{\mathrm{d}t} = M(t) \times \gamma B(t) \tag{1.8}$$

where $\boldsymbol{B} = (B_x, B_y, B_z)$ represents the three orthogonal magnetic fields. B_x and B_y are part of the oscillatory magnetic field of the RF pulse and B_z represents the static magnetic field B_0. Expanding the cross product in Eq. (1.8) yields three coupled differential equations (see Exercises for more detail) for the three components of $\boldsymbol{M}$ that are given by

$$\frac{\mathrm{d}M_x(t)}{\mathrm{d}t} = \gamma M_y(t) B_0 - \gamma M_z(t) \mathrm{B}_{1y} \tag{1.9}$$

$$\frac{\mathrm{d}M_y(t)}{\mathrm{d}t} = \gamma M_z(t) B_{1x} - \gamma M_x(t) B_0 \tag{1.10}$$

$$\frac{\mathrm{d}M_z(t)}{\mathrm{d}t} = \gamma M_x(t) B_{1y} - \gamma M_y(t) B_{1x} \tag{1.11}$$

Equations (1.9)–(1.11) (or the compact form of Eq. (1.8)) describe Larmor precession of the nuclear magnetization $\boldsymbol{M}$ in an external magnetic field B_0, as well as the rotation of $\boldsymbol{M}$ by a time-varying RF field with components B_{1x} and B_{1y}. The presence of relaxation requires an additional term to Eqs. (1.8)–(1.11) that describes the disappearance of magnetization from the transverse plane due to T_2 relaxation and the reappearance of the thermal equilibrium magnetization M_0 due to T_1 relaxation.

$$\frac{\mathrm{d}M_x(t)}{\mathrm{d}t} = -\frac{M_x(t)}{T_2} \tag{1.12}$$

$$\frac{\mathrm{d}M_y(t)}{\mathrm{d}t} = -\frac{M_y(t)}{T_2} \tag{1.13}$$

$$\frac{\mathrm{d}M_z(t)}{\mathrm{d}t} = -\frac{M_z(t) - M_0}{T_1} \tag{1.14}$$

Adding Eqs. (1.9)–(1.11) and (1.12)–(1.14) provides the complete Bloch equations in the nonrotating, laboratory frame. Simple solutions are readily obtained for the transverse magnetization following excitation and T_1 and T_2 relaxation in the absence of an RF field (see Exercises). A general solution typically requires numerical integration, although analytical solutions have been obtained for specific RF driving functions. In Chapter 5 it will be shown that in the absence of relaxation, the Bloch equations can be reduced to 3×3 rotation matrices. Under many circumstances NMR experiments are more conveniently described in a Cartesian frame that is rotating around the main magnetic field B_0 at the frequency ν of the B_1 field. Transformation of the Bloch equations from the laboratory frame to the rotating frame (see Exercises) yields

$$\frac{\mathrm{d}M'_x(t)}{\mathrm{d}t} = (\omega_0 - \omega)M'_y(t) - \frac{M'_x(t)}{T_2} \tag{1.15}$$

$$\frac{\mathrm{d}M'_y(t)}{\mathrm{d}t} = -(\omega_0 - \omega)M'_x(t) + \gamma B_1 M'_z(t) - \frac{M'_y(t)}{T_2} \tag{1.16}$$

$$\frac{\mathrm{d}M'_z(t)}{\mathrm{d}t} = -\gamma B_1 M'_y(t) - \frac{M'_z(t) - M_0}{T_1} \tag{1.17}$$

Equations (1.15)–(1.17) quantitatively describe the features that were qualitatively described with the introduction of rotating frames (Figure 1.5). In the rotating frame the RF field B_1 is along the x' axis and thus does not affect M'_x. In addition, the large B_0 magnetic field (or large $\omega_0 = \gamma B_0$ angular frequency offset) is reduced to $(\omega_0 - \omega)$ or even zero when the RF frequency ω and Larmor frequency ω_0 are exactly matched. In the on-resonance condition ($\omega = \omega_0$) the transverse magnetization does not precess over time and in the absence of an RF pulse only decays due to T_2 relaxation. The Bloch equations provide a quantitative description of any NMR experiment that involves RF pulses and relaxation on a sample of noninteracting spins (i.e. without scalar coupling). Modifications of the Bloch equations to include the effects of diffusion and chemical exchange give rise to the Bloch–Torrey [42] and Bloch–McConnell [43] equations, respectively.

1.8 Fourier Transform NMR

The FID of a sample with a single Larmor frequency following excitation into the transverse plane of the laboratory frame (Figure 1.7) can be obtained by solving the Bloch equations of Eqs. (1.9)–(1.14). The resulting FID signal can be described with a complex function $f(t) = R(t) + iI(t)$, where the real $R(t)$ and imaginary $I(t)$ components are given by (see Exercises)

$$R(t) = M_x(t) = M_0 \cos(2\pi\nu_0 t + \phi)\mathrm{e}^{-t/T_2^*} \tag{1.18}$$

$$I(t) = M_y(t) = -M_0 \sin(2\pi\nu_0 t + \phi)\mathrm{e}^{-t/T_2^*} \tag{1.19}$$

where ϕ represents the phase of the transverse magnetization relative to the x axis immediately following excitation. For an excitation pulse along the x axis, the transverse magnetization is excited along the y axis, making the phase ϕ equal to −90°. It follows that the FID is described by four independent parameters, M_0, ν_0, T_2^*, and ϕ, whereby it is assumed that the sample was in a state of thermal equilibrium before excitation. All four parameters describing the FID can be easily recognized in the case of a single Larmor frequency (Figure 1.8A). Especially, the M_0 parameter is of great importance in many NMR applications as it is directly related to the concentration (Eq. (1.4)). For a single frequency signal, M_0 is proportional to the intensity of FID immediately following excitation.

As will be discussed in Section 1.9, one of the strengths of NMR is that different compounds and different chemical groups within a compound can be identified based on differences in their Larmor frequencies. In the case of multiple frequencies, the deduction of the four parameters for each signal will prove difficult, if not impossible, by visual inspection of a time-domain FID signal (Figure 1.8G). Fortunately, a standard processing tool exists that allows the extraction and separation of different frequencies from a time-domain FID and presents it as signals

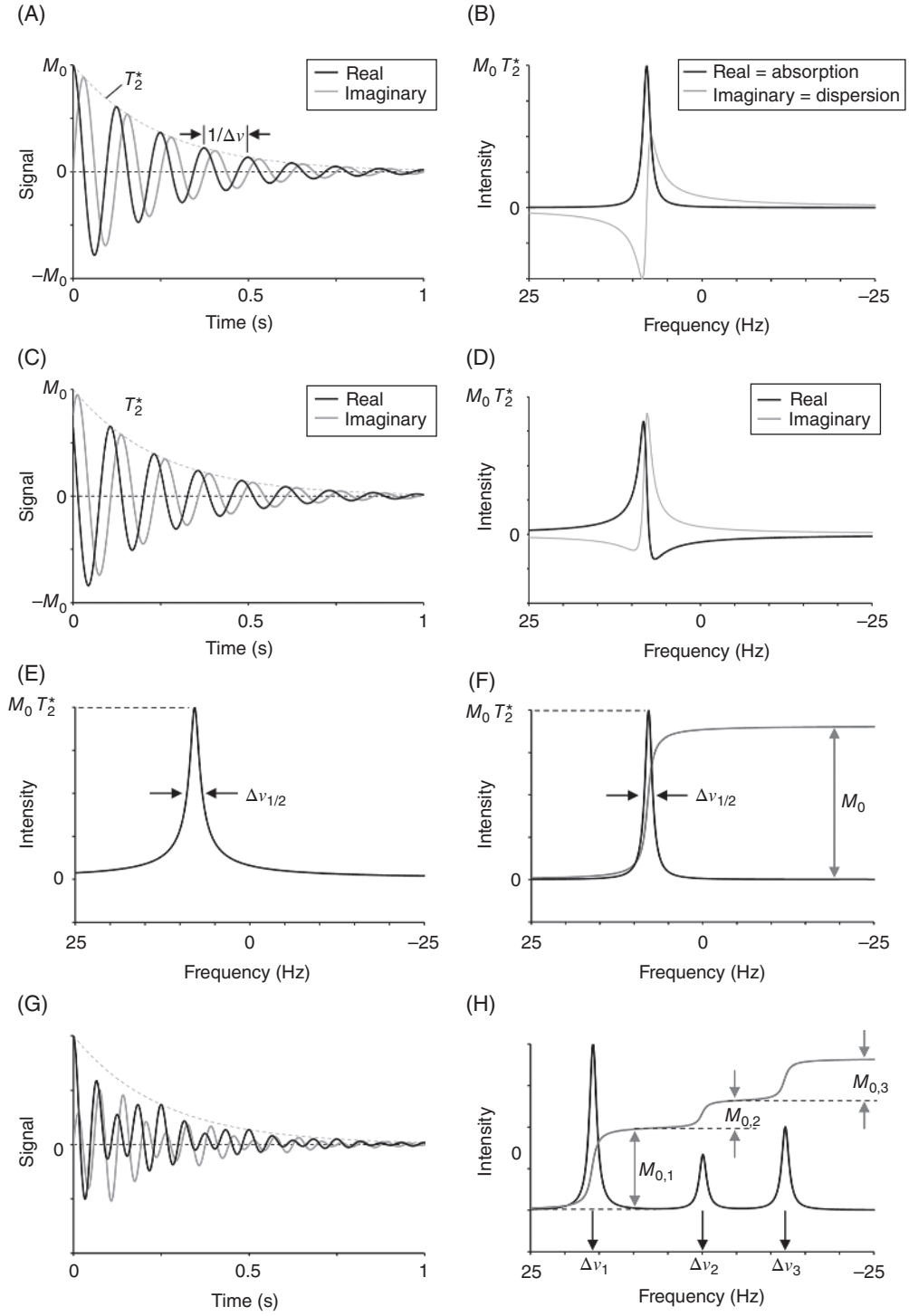

Figure 1.8 Fourier transformation of time and frequency-domain signals. (A) Complex, exponentially-decaying, single-frequency FID as described by four parameters M_0, $\Delta\nu$, T_2^*, and ϕ. The phase ϕ is defined as the angle of the transverse magnetization at the start of signal acquisition. (B) FT of the time-domain FID gives a complex, frequency-domain spectrum. By convention only the real part of the spectrum (black line) is shown. When $\phi = 0$, the real spectrum equals the absorption spectrum. (C, D) When $\phi \neq 0$, the real (and imaginary) spectrum represents a mixture of absorptive and dispersive lines according to Eqs. (1.21) and (1.22). The dispersive contribution is undesirable due to the long "tails" and can be eliminated through zero-order phase correction (see text for details). (E) A magnitude representation of the frequency-domain spectrum (Eq. (1.26)) can be used to eliminate all phase information, but comes at the expense of an increase line width $\Delta\nu_{1/2}$. (F) The peak height and integral of the absorption spectrum are proportional to $M_0T_2^*$ and M_0, respectively, whereby the line width $\Delta\nu_{1/2}$ equals $1/(\pi T_2^*)$. (G, H) Fourier transformation of a multifrequency time-domain signal (G) readily reveals the frequency components and amplitude in the frequency-domain (H).

in a frequency-domain spectrum. The Fourier transformation calculates a frequency-domain spectrum $F(\nu)$ from a time-domain signal $f(t)$ according to

$$F(\nu)=\int_{-\infty}^{+\infty} f(t)\mathrm{e}^{-2\pi i\nu t}\mathrm{d}t \tag{1.20}$$

whereby the time-domain FID, $f(t) = R(t) + iI(t)$ is given by Eqs. (1.18) and (1.19). For an FID signal the integration boundaries run from 0 to $+\infty$. The Fourier transformation is a reversible operation, such that the inverse Fourier transformation of the spectrum $F(\nu)$ yields the original time-domain function $f(t)$. Since the integral of Eq. (1.20) involves a complex exponential, the frequency-domain spectrum $F(\nu) = R(\nu) + iI(\nu)$ will also be complex. The real and imaginary components are given by (see Exercises)

$$R(\nu)=A(\nu)\cos\phi-D(\nu)\sin\phi \tag{1.21}$$

$$I(\nu)=D(\nu)\cos\phi+A(\nu)\sin\phi \tag{1.22}$$

whereby the absorption $A(\nu)$ and dispersion $D(\nu)$ spectral components are given by

$$A(\nu)=\frac{M_0T_2^*}{1+4\pi^2(\nu_0-\nu)^2T_2^{*2}} \tag{1.23}$$

$$D(\nu)=\frac{2\pi M_0(\nu_0-\nu)T_2^{*2}}{1+4\pi^2(\nu_0-\nu)^2T_2^{*2}} \tag{1.24}$$

The curves described by Eqs. (1.23) and (1.24) are collectively known as a Lorentzian line shape. Figure 1.8B shows the real and imaginary spectra obtained following Fourier transformation of the FID signal shown in Figure 1.8A. When the phase ϕ equals zero, the real spectrum reduces to the absorption spectrum ($R(\nu) = A(\nu)$) and the imaginary spectrum reduces to the dispersion spectrum ($I(\nu) = D(\nu)$). However, in general, the phase is not zero and the spectrum will be a mixture of absorption and dispersion spectra (Figure 1.8C and D). From Figure 1.8B and D it is clear that the dispersion spectrum is not desirable as it has broad "tails" that span over a much wider spectral range than the absorption spectrum. In case of multiple signals the dispersive part of the spectrum will display a much larger amount of overlap between signals than the absorptive part. Zero-order phase correction is a standard routine available on any spectrometer that aims at minimizing the dispersive component in the real spectrum such that the real spectrum equals the absorption spectrum. Zero-order phase correction is most easily performed in the time domain, by recognizing that the time-domain FID given by Eqs. (1.18) and (1.19) can be written as a complex exponential using Euler's formula (see Appendix A.2)

$$f(t)=M_0\mathrm{e}^{-2\pi i\nu_0 t}\mathrm{e}^{-t/T_2^*}\mathrm{e}^{i\phi} \tag{1.25}$$

By multiplying the FID signal with a zero-order phase correction $\mathrm{e}^{-i\phi_c}$, the phase can be removed from the FID and the resulting spectrum when $\phi = \phi_c$. Under certain conditions, when zero-order phase correction is not available or viable, the phase of the spectrum can be removed by calculating the absolute-valued or magnitude spectrum (Figure 1.8E) according to

$$|F(\nu)|=\sqrt{R(\nu)^2+I(\nu)^2} \tag{1.26}$$

Since the magnitude spectrum holds both real and imaginary components, it is always broader than the corresponding, phased absorption spectrum (Figure 1.8F).

The four parameters describing the time-domain FID can also be recognized in the absorption spectrum. The first point of the FID, M_0, equals the area under the curve of the absorption spectrum and can be obtained by numerical integration (summation) of the spectrum (Figure 1.8F). Note that the peak height of a Lorentzian line is equal to $M_0T_2^*$. While it is attractive to use peak height as a substitute for relative M_0 between various signals, it has to be used with great caution as a change in T_2^* can change the relative peak heights without a true change in M_0. The oscillation or frequency ν_0 of the signal can be recognized as the horizontal position on the frequency axis. The T_2^* relaxation time can be obtained from the frequency width at half the peak height, $\Delta\nu_{1/2}$ according to

$$\Delta\nu_{1/2} = \frac{1}{\pi T_2^*} \tag{1.27}$$

Whereas Figure 1.8A–F dealt with single-frequency signals that could have been analyzed in the time domain, the power of Fourier transformation becomes indispensable when multifrequency signals are acquired. Figure 1.8G shows an FID containing three different frequencies with different amplitudes M_0. While it is apparent that more than one frequency is involved, it is not obvious how to extract the different parameters for each signal in the time domain. Following Fourier transformation, the spectrum in Figure 1.8H immediately reveals the three distinct frequencies, whereas spectral integration gives the relative M_0 amplitudes.

1.9 Chemical Shift

In the years following the discovery of NMR, the technique was primarily used by the physics community. As the Larmor frequency of a given nucleus only depended on the external magnetic field strength, according to Eq. (1.1), it provided physicists the opportunity to measure the magnetic moments of different nuclei with unprecedented precision. At this point in time NMR was of little interest to chemists. That all changed by a number of papers published in 1950 and 1951 that demonstrated different resonance frequencies for various chemical groups within the same molecule. Proctor and Yu [7] described two distinct ^{14}N resonances in an ammonium nitrate (NH_4NO_3) solution, whereas Dickinson [8] described the dependence of ^{19}F resonance frequencies on chemical composition. The ability of NMR to provide detailed chemical information on compounds was firmly established when Arnold et al. [9] in 1951 published a high-resolution ^{1}H NMR spectrum of ethanol in which separate signals from methyl, methylene, and hydroxyl protons could be clearly recognized. This effect, in which the local chemical environment surrounding a nucleus influences the resonance frequency, is known as the chemical shift.

The phenomenon of chemical shift is caused by a shielding of the magnetic field at the nucleus by the surrounding electron cloud. Figure 1.9A shows a hypothetical, single proton in an external magnetic field B_0. The magnetic field experienced by the nucleus, B_n, is identical to the external magnetic field B_0 and the ^{1}H Larmor frequency is given by Eq. (1.1). The hypothetical, single proton would normally be surrounded by an electron cloud (Figure 1.9C). Classically, the electron cloud can be seen as a current rotating around the nucleus, which then generates a magnetic field B_e at the nucleus that opposes the external magnetic field B_0. The magnetic field B_n at the nucleus, being the sum of B_0 and B_e, is thus reduced relative to Figure 1.9A leading to a lower Larmor resonance frequency (Figure 1.9D). In general, the proton in Figure 1.9C is part of a larger molecule and is bound directly to a carbon or other

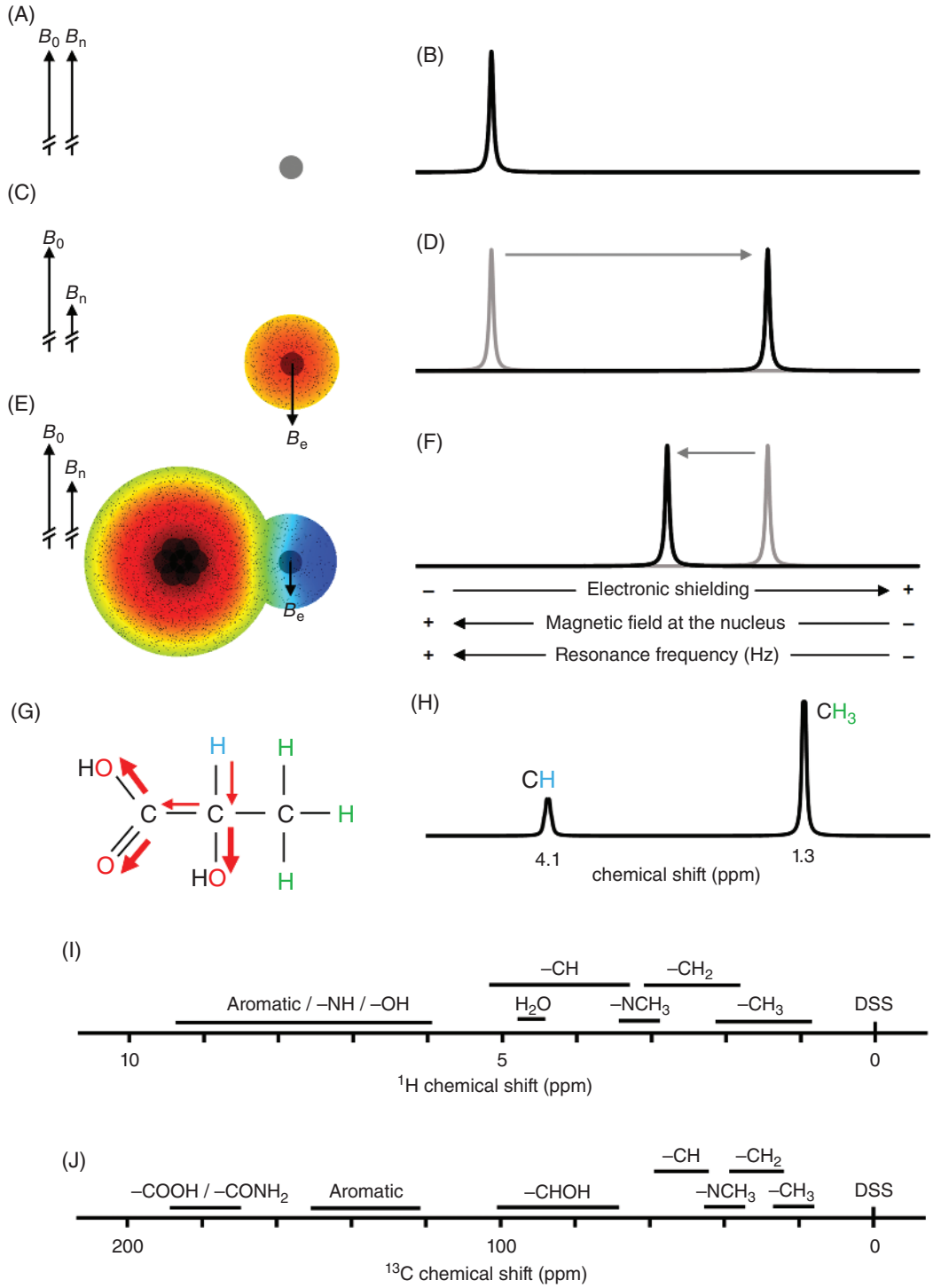

Figure 1.9 Origin of the chemical shift. (A) The magnetic field B_n at the nucleus of a single proton is equal to the external magnetic field B_0 leading to (B) a spectrum with a signal at Larmor frequency $\nu_0 = (\gamma/2\pi)B_0 = (\gamma/2\pi)B_n$. (C) The electron density in a hydrogen atom can be regarded as small currents that generate a magnetic field B_e that opposes B_0. The magnetic field at the nucleus is therefore reduced, (D) leading to a lower Larmor frequency. (E, F) The electron density of hydrogen in larger molecules depends on the electronegativity of nearby atoms, such that the exact Larmor frequency becomes very sensitive to the chemical environment. (G, H) The electronegative oxygen atoms in lactate shift the electron density away from the protons, leading to reduced electronic shielding. Since the single methine proton is closer to electronegative oxygen atoms than the three methyl protons, its Larmor frequency and chemical shift are higher. (I, J) Chemical shift ranges from various chemical groups as detected with (I) ^{1}H NMR and (J) ^{13}C NMR. The methyl protons of DSS (2,2-dimethyl-2-silapentane-5-sulfonate) are assigned a chemical shift $\delta = 0$.

atom (Figure 1.9E). Most atoms in organic compounds, like carbon, nitrogen, and oxygen, have a stronger electronegativity than protons meaning that they tend to pull electron cloud density away from protons. As the electron cloud density surrounding the proton decreases, so does the electron-induced magnetic field B_e. The total magnetic field at the nucleus B_n will therefore be larger than in Figure 1.9C leading to a higher proton resonance frequency (Figure 1.9F). The effect of chemical shift can be included in the Larmor Eq. (1.1) by understanding that B_0 means the magnetic field *at* the nucleus B_n, which includes besides the main magnetic field also shielding effects.

Using the arguments laid out for Figure 1.9A–F, the ^{1}H NMR spectrum of lactic acid (Figure 1.9G) can be qualitatively understood. Lactic acid has four types of protons in the methyl, methine, hydroxyl, and carbonyl groups. When lactic acid is dissolved in water, the hydroxyl and carbonyl protons undergo fast exchange with the water protons making them effectively invisible in a normal ^{1}H NMR spectrum (see Chapter 3 for more details on chemical exchange). The methyl and methine protons give rise to resonance lines at lower and higher Larmor resonance frequencies, respectively. The methyl protons have a relatively high electron cloud density due to the absence of atoms with a high electronegativity, like oxygen, in the immediate vicinity. The high electronic shielding leads to a lower magnetic field at the nucleus and hence a lower Larmor resonance frequency. The electron density around the methine proton is much lower due to the presence of three oxygen atoms within two to three chemical bonds. As a result, the magnetic field at the nucleus and thus the Larmor resonance frequency is higher. This assignment can be confirmed by noting that the relative signal areas of the high- and low-frequency signals are 1 and 3, corresponding to the single methine and three methyl protons.

The Larmor resonance frequencies have so far been expressed in units of Hertz (Hz), based on the Larmor Eq. (1.1). However, for chemical identification and comparisons between laboratories this proves to be an inconvenient choice as the Larmor frequency (in Hz) is dependent on the external magnetic field B_0 (in T). The Larmor resonance frequency can become independent of the magnetic field strength when expressed in parts-per-million (ppm) relative to a reference compound according to

$$\delta = \frac{\nu - \nu_{\text{ref}}}{\nu_{\text{ref}}} \times 10^6 \tag{1.28}$$

where δ is referred to as the chemical shift (in ppm) and ν and ν_{ref} are the Larmor frequencies (in Hz) of the compound under investigation and of a reference compound, respectively.

The reference compound should ideally be chemically inert and its chemical shift should be independent of external variables (temperature, ionic strength, shift reagents) and produce a strong (singlet) resonance signal well separated from all other resonances. A widely accepted reference compound for ^{1}H and ^{13}C NMR is tetramethylsilane (TMS) to which $\delta = 0$ has been assigned. However, the use of TMS is restricted to NMR on compounds in organic solvents. For aqueous solutions, 3-(trimethylsilyl)propionate (TSP) or 2,2-dimethyl-2-silapentane-5-sulfonate (DSS) is typically used, of which DSS is more desirable as the chemical shift is temperature and pH independent [44]. Unfortunately, none of these compounds are found in *in vivo* systems and can therefore never be used as internal references. TSP and DSS can in principle be used as an external reference compound, being placed adjacent to the object under investigation. However, under these circumstances the observed chemical shift needs to be corrected for bulk magnetic susceptibility effects as well as macroscopic inhomogeneity of the main magnetic field (see Chapter 10). Differences in susceptibility and local magnetic field strength between the object under investigation and the adjacent external

reference make the use of external chemical shift referencing undesirable. For *in vivo* applications other resonances have been used as an internal reference. Commonly used internal references are the methyl resonance of *N*-acetyl aspartate (2.01 ppm) for ^{1}H MRS of the brain and the phosphocreatine resonance (0.00 ppm) for ^{31}P MRS of brain and muscle. The International Union of Pure and Applied Chemistry (IUPAC) recommends the use of universal referencing for *any* NMR nucleus based on the proton Larmor frequency of DSS [45]. This excellent recommendation is currently only viable under the highly controlled conditions encountered with high-resolution, liquid-state NMR.

Figure 1.9I and J provide an overview of the chemical shifts observed for common chemical groups with ^{1}H and ^{13}C NMR. The overall pattern can be qualitatively explained by shielding effects due to neighboring electronegative atoms. In many NMR publications the terms "downfield" and "upfield" are encountered when the chemical shift of one signal is expressed relative to another signal. The origin of these terms can be found in the early days of NMR in which a spectrum was obtained by varying the magnetic field through a fixed frequency RF source. Signals with a high Larmor frequency and hence a high chemical shift required a lower magnetic field to be in resonance with the fixed frequency RF source. In the NMR spectrum, in which the horizontal axis was expressed in Tesla, signals with a high Larmor frequency would appear "downfield" from signals with a lower Larmor frequency. In modern NMR experiments where the magnetic field is constant the terms "downfield" and "upfield" are confusing. However, since the terms see continued usage in modern NMR literature, one could reinterpret them as reduced and increased electronic shielding fields B_e at the nucleus for "downfield" and "upfield," respectively. In Figure 1.9I and J the resonances in or adjacent to electronegative moieties, such as carbonyl and hydroxyl groups, appear in the downfield region of the spectrum, whereby highly shielded methyl groups appear in the upfield region.

1.10 Digital NMR

The NMR signal as presented up to this point and as detected by Bloch in 1946 is a continuous, analog signal. While acceptable for scanning 1D MR spectra, analog acquisition and processing of NMR signals are incompatible with modern multidimensional NMR and MRI experiments. Since the revolutions in NMR (FT NMR, 2D NMR, MRI) ran parallel to the development of modern computing, NMR could take full advantage of all the benefits provided by digital acquisition and processing.

1.10.1 Analog-to-Digital Conversion

The first step in bringing NMR into the digital domain is the conversion of the analog FID signal induced in a receiver coil into a digital signal. This is achieved with an analog-to-digital converter (ADC), which measures the instantaneous value of the FID at equal time intervals (Figure 1.10). The speed of the analog-to-digital conversion is prescribed by the sampling theory [46, 47]. This theory states that any sinusoidal signal of frequency F can be accurately described when it is sampled at least twice per cycle. This minimum sampling rate is called the Nyquist frequency F_N. The spectral bandwidth SW equals $2F_N$, since frequencies between $-F_N$ and $+F_N$ are accurately sampled. The time between the data points, Δt (Figure 1.10B), is known as the dwell time and equals 1/SW. If a signal is present with a frequency greater than the Nyquist frequency, then this signal will still be digitized, but at an incorrect frequency (Figure 1.10E). A resonance with frequency $\nu_{real} = F_N + \Delta\nu$ relative to the center of the spectral bandwidth will appear after Fourier transformation at an apparent position with frequency $\nu_{app} = -F_N + \Delta\nu$.

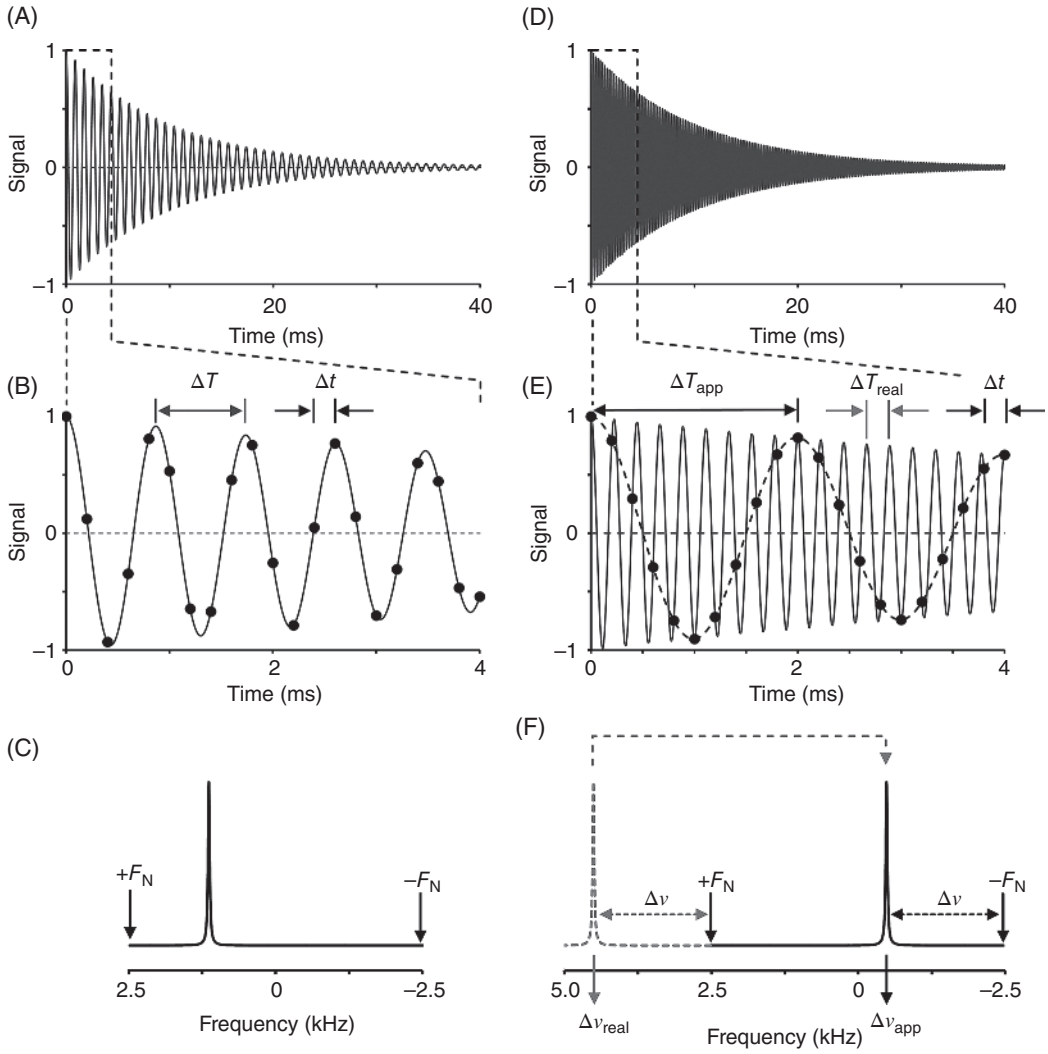

Figure 1.10 Analog-to-digital conversion and signal aliasing. (A) Time-domain FID signal with a frequency $\Delta\nu$ of 1.15 kHz acquired over a spectral bandwidth (SW) of 5.0 kHz, making the Nyquist sampling frequency $F_N = SW/2$. (B) The analog-to-digital converter (ADC) samples the signal at each dwell-time $\Delta t = 1/SW = 0.2$ ms (black dots). Since each period of the signal $\Delta T = 1/\Delta\nu$ is sampled multiple times by the ADC (i.e. $\Delta t < \Delta T$) the Nyquist sampling condition is satisfied, giving (C) a spectrum with the proper frequency. (D) Time-domain FID signal with a frequency $\Delta\nu_{real} = \Delta\nu + F_N$ of 4.5 kHz. (E) Each period ΔT_{real} of the signal is sampled less than twice (i.e. $\Delta t > \Delta T_{real}$) by the ADC such that the Nyquist sampling condition is not satisfied. The sampled data points do still represent a sinusoidal signal, but are sampled at an apparent, lower frequency with period ΔT_{app}. (F) Following Fourier transformation the signal is aliased, appearing at an apparent frequency $\Delta\nu_{app} = \Delta\nu - F_N = -0.5$ kHz.

This so-called aliasing of resonances can lead to erroneous identification of signals. Aliasing can easily be avoided by increasing the spectral bandwidth (i.e. decreasing the dwell time Δt), after which the minimum spectral bandwidth needed to unambiguously observe all the resonances can be determined. Aliasing of signal seems at first sight a large problem in FT NMR, since noise from outside the spectral region would be folded back into the spectrum thereby dramatically

decreasing the obtainable S/N ratio. However, high-frequency noise components can easily be filtered out before the ADC sampling by bandpass filters (see Chapter 10). A cut-off filter, such as a Butterworth filter does not affect signals within the spectral range, while suppressing (i.e. multiplying by zero) all signals (i.e. noise) outside the spectral range. In this case, real NMR signals outside the spectral bandwidth will also be suppressed and will therefore be absent in the final NMR spectrum. Aliasing is readily observed in applications where frequencies are sampled indirectly, such as the phase-encoding directions in MR imaging and spectroscopic imaging (see Chapters 4 and 7) and the second dimension in 2D NMR (see Chapter 8).

1.10.2 Signal Averaging

Once the NMR signal is digitized, it can be stored in memory for processing or signal averaging. In signal averaging the signal-to-noise ratio (SNR) of the FID is improved by adding or averaging the FID signals of several consecutive, identical experiments. Averaging of n FID signals leads to an improvement in SNR of a factor $\sqrt{n}$ [48, 49]. This is because the voltage of the signal S increases linearly with n, while for the random processes of noise N the power increases linearly. Since power is proportional to the square of voltage, the noise voltage increases as $\sqrt{n}$, leading to an overall improvement of the SNR of $n/\sqrt{n} = \sqrt{n}$. In practice, the improvement in SNR for *in vivo* NMR by time-averaging is limited, since an improvement of a factor 10 requires a prolongation of measurement time by a factor $10^2 = 100$. Typically, an *in vivo* NMR experiment is a compromise between sufficient SNR and the allowable duration of the experiment.

1.10.3 Digital Fourier Transformation

The stored, digital FID signal can be processed by Fourier transformation to produce a digital MR spectrum. The analog Fourier transformation (Eq. (1.20)) which entails a continuous integration is then replaced with a digital or discrete Fourier transformation (DFT) composed of a discrete summation. However, direct computation of a discrete summation is very inefficient, requiring N^2 calculations for a signal containing N data points. For 1D MR spectra direct summation may be acceptable, but for larger 2D and 3D MRI and MRSI datasets, direct summation would lead to unacceptable calculation times. By using symmetry and recursive characteristics of DFT, Cooley and Tukey [50] proposed in 1965 a new algorithm for the special case of N being a power of 2. This fast Fourier transform (FFT) algorithm requires only $N \log_2 N$ calculations, leading to a 32-fold reduction in calculation time for a dataset with $N = 256$. The improvement increases to 1024 for a MR image with a standard 256×256 matrix. Whereas modern FFT algorithms now also give substantial improvements for powers other than 2, MR images often continue to be acquired on a "power of 2" matrix size.

1.10.4 Zero Filling

In general, the FID of a spectrum with spectral width $SW = 2F_N$ is sampled by the ADC over N points spaced by the dwell time $\Delta t = 1/SW$. The total duration of signal acquisition, T_{acq}, is therefore $N \times \Delta t$. Following Fourier transformation of the FID, the NMR spectrum will also contain N points spread out over the spectral width SW. The spectral digital resolution is therefore SW/N, which is equivalent to the reciprocal of the total acquisition, i.e. $1/T_{acq}$. For an experiment with 256 points sampled and $T_{acq} = 64$ ms (Figure 1.11A), leading to $SW = 2F_N = 4.0$ kHz, the spectral resolution is 15.63 Hz per point. When the digital Fourier transform spectrum (Figure 1.11B) is compared to the continuous Fourier transform spectrum it is clear that the digital resolution is

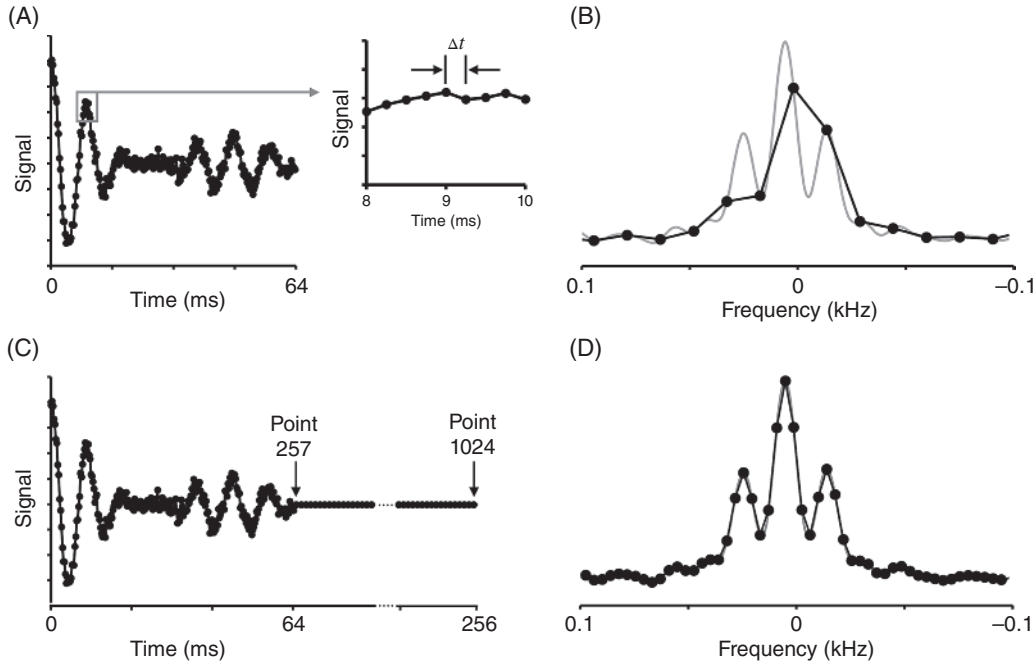

Figure 1.11 Zero filling and spectral resolution. (A) Time-domain FID signal acquired and digitized as 256 points over a spectral width of 4.0 kHz (i.e. $\Delta t = 0.25$ ms). (B) Fourier transform spectrum of the digitized time-domain FID signal (black) compared to an analog spectrum (gray). The limited digital resolution of 15.63 Hz per point prevents the visualization of all spectral features. (C) Adding an additional 768 points of zero amplitude to the experimental data, known as zero filling, leads (D) to an increased spectral resolution of 3.91 Hz per point upon Fourier transformation. Zero filling leads to an improved visualization of the spectral features that were already present in the digitized data of (A).

insufficient to properly visualize all spectral features. The digital resolution can be improved by increasing the total acquisition time T_{acq}. This can be achieved by decreasing the spectral width, SW, or increasing the number of acquisition points, N. A decrease in the spectral bandwidth is often limited by the minimum width required to avoid aliasing. Increasing the number of acquisition points comes at the cost of a decreased SNR as more noise and less signal are acquired. The process of extending the acquisition time can be simulated during post-acquisition processing by extending the acquired FID (which has decayed to zero amplitude) artificially by adding a string of points with zero amplitude to the FID prior to (discrete) Fourier transformation (Figure 1.11C). This process is known as zero filling and while it does not increase the information content of data, it can greatly improve the visual appearance of spectra (Figure 1.11D).

1.10.5 Apodization

The appearance of an NMR spectrum can often be improved when the Fourier transformation is combined with additional processing steps. Zero filling was shown to be an effective tool to enhance the digital resolution and visualize all features of NMR spectra (Figure 1.11). Apodization (or time-domain filtering) is another tool used prior to Fourier transformation to enhance the SNR and/or spectral resolution of spectra. During apodization the time-domain FID signal, $f(t)$, is multiplied with a filter function, $f_{filter}(t)$. Common filter functions are exponential weighting

$$f_{\text{filter}}(t) = \mathrm{e}^{-t/T_{\mathrm{L}}} \tag{1.29}$$

or a Lorentzian-to-Gaussian transformation

$$f_{\text{filter}}(t) = \mathrm{e}^{+t/T_{\mathrm{L}}}\mathrm{e}^{-t^2/T_{\mathrm{G}}^2} \tag{1.30}$$

where T_{L} and T_{G} are user-adjustable parameters. A decreasing mono-exponential filter function according to Eq. (1.29) with $T_{\mathrm{L}} > 0$ improves the SNR of the spectrum since the data points at the end of the FID containing primarily noise are attenuated (Figure 1.12B). An unavoidable side effect is that the filter function causes the FID signal to decay faster than the natural T_2^*, leading to a faster, apparent $T_{2,\mathrm{app}}^*$ relaxation time constant ($(T_{2,\mathrm{app}}^*)^{-1} = (T_2^*)^{-1} + (T_{\mathrm{L}})^{-1}$) and hence broader resonance lines (Eq. (1.29), Figure 1.12B). As a result, time-domain apodization with a decreasing exponential function is colloquially referred to as "line broadening the spectrum."

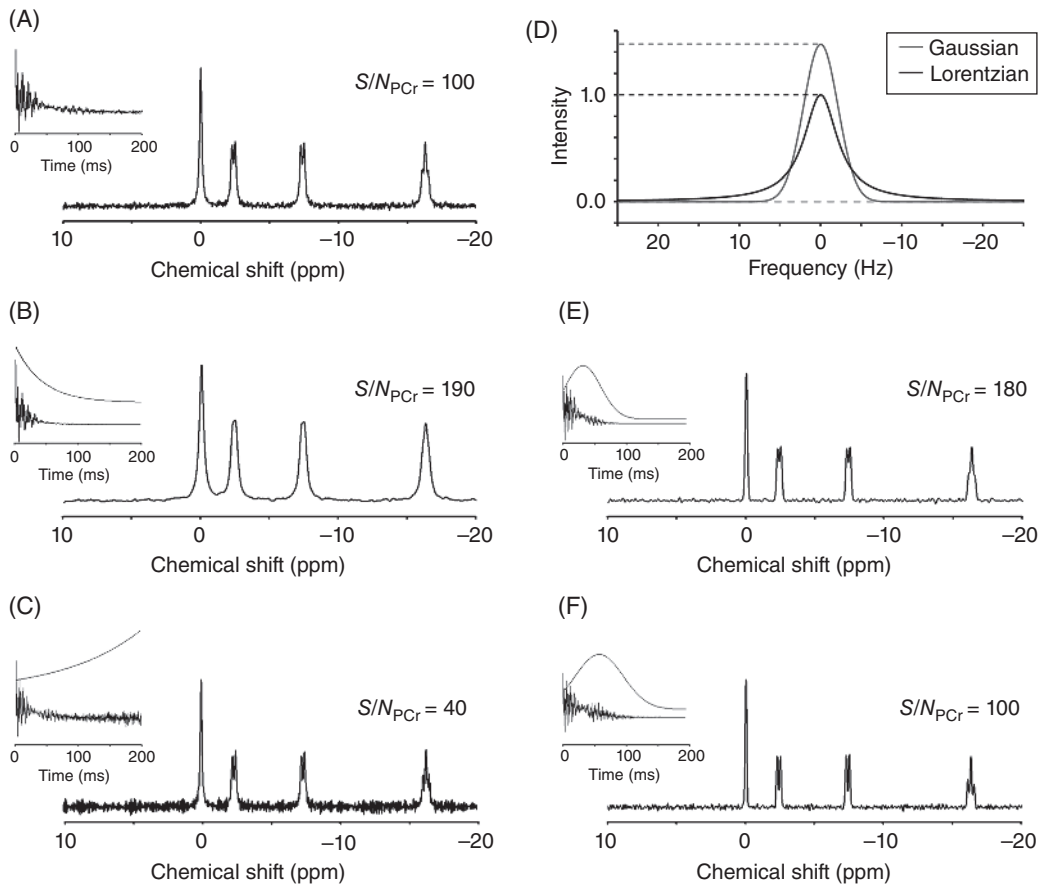

Figure 1.12 Time-domain apodization. (A) Time and frequency domain signal of ^{31}P-containing phantom (PCr and ATP) processed without apodization. (B) Time-domain multiplication with a decaying exponential function leads to increased SNR at the expense of spectral resolution. (C) Apodization with an increasing exponential improves the spectral resolution but comes with an SNR penalty. (D) Gaussian and Lorentzian line shapes with identical line widths (at half maximum) and integrated intensities. (E, F) Lorentzian-to-Gaussian transformation with T_{L} and T_{G} parameters optimized to provide (E) improved SNR at identical spectral resolution compared to (A) and (F) improved spectral resolution while maintaining the same SNR.

When sufficient data has been recorded to minimize truncation artifacts ($T_{acq} > 3T_2^*$), then optimal sensitivity is obtained by using a so-called matched filter in which $T_L = T_2^*$. The improved SNR comes at the expense of a doubling of the spectral line widths, i.e. spectral resolution has been traded for sensitivity. Besides improving the SNR, this apodization can also be used on FIDs where the last data points have been truncated resulting in oscillatory artifacts in the frequency domain. For $T_L < 0$ the apodization according to Eq. (1.29) leads to a resolution enhancement, since the apparent T_2^* becomes longer, resulting in line narrowing (Figure 1.12C). However, the SNR is decreased since the data points at the end of the FID with a relatively high noise contribution are emphasized.

The Lorentzian-to-Gaussian filtering function (Eq. (1.30)) converts a Lorentzian line shape to a Gaussian line shape. A Gaussian line shape decays to the baseline in a narrower frequency range as would a Lorentzian line shape with the same line width at half height. In other words, a Lorentzian line shape produces longer "tails" that are a disadvantage when accurate determination (by integration) of overlapping resonance lines is required (Figure 1.12D). The principle of the Lorentzian-to-Gaussian transformation is to cancel (or decrease) the Lorentzian part of the FID (by multiplying with $\exp(+t/T_L)$, where $T_L = T_2^*$, such that $\exp(+t/T_L)\cdot\exp(-t/T_2^*) = 1$) while increasing the Gaussian character of the FID (by multiplying with $\exp(-t^2/T_G^2)$). Using a sufficiently long T_G value, significant resolution enhancement can be achieved. Figure 1.12E shows the process of time-domain filtering on a ^{31}P FID. Even though an increasing exponential filter (Figure 1.12C) and a Lorentzian-to-Gaussian transformation can achieve the same resolution enhancement, the former is accompanied by a significant decrease in sensitivity, which can be minimized with a Lorentzian-to-Gaussian transformation. In fact, the two adjustable parameters in Eq. (1.30) can be used to improve the SNR without a significant decrease in spectral resolution (Figure 1.12E) or to improve the spectral resolution without a significant decrease in sensitivity (Figure 1.12F). Besides the mentioned, most commonly used apodization functions, a wide range of other functions are available each with specific characteristics regarding sensitivity and resolution [51].

1.11 Quantum Description of NMR

The description of NMR presented so far has largely followed the classical treatment laid out by Bloch [2–4]. Besides the fact that nuclear spin is an intrinsic quantum property, the classical vector model did not rely on quantum mechanics and was able to provide a physically intuitive description of NMR. However, NMR can also be approached from a quantum mechanical point of view as was done by Purcell and colleagues [1]. One of the fundamentals of quantum mechanics is that energy, momentum, and other properties are quantized, meaning that they are restricted to specific, discrete values. Transitions between discrete energy levels can be investigated with spectroscopy, which in general terms is the study of the interaction between matter and electromagnetic radiation. For example, IR spectroscopy investigates energy-level transitions associated with different vibrational modes (Figure 1.13A). As the name implies, IR spectroscopy uses electromagnetic waves in the IR part of the electromagnetic spectrum (10^{12}–10^{14} Hz). Different vibrational modes are characterized by quantized energy levels given by $E = (n + ½)h\nu$, where n is an integer quantum number ($n = 0, 1, 2, \ldots$) corresponding to the separate levels. There are two primary modes to "sample" the energy-level differences, by absorption or by emission. Molecules that vibrate at a lower energy level with quantum number n can move to a higher energy level with quantum number $(n + 1)$ by *absorption* of electromagnetic energy with a frequency ν that exactly matches the energy-level difference ΔE, according to $\Delta E = h\nu$. Conversely, a molecule with high vibrational energy can drop down to a lower vibrational

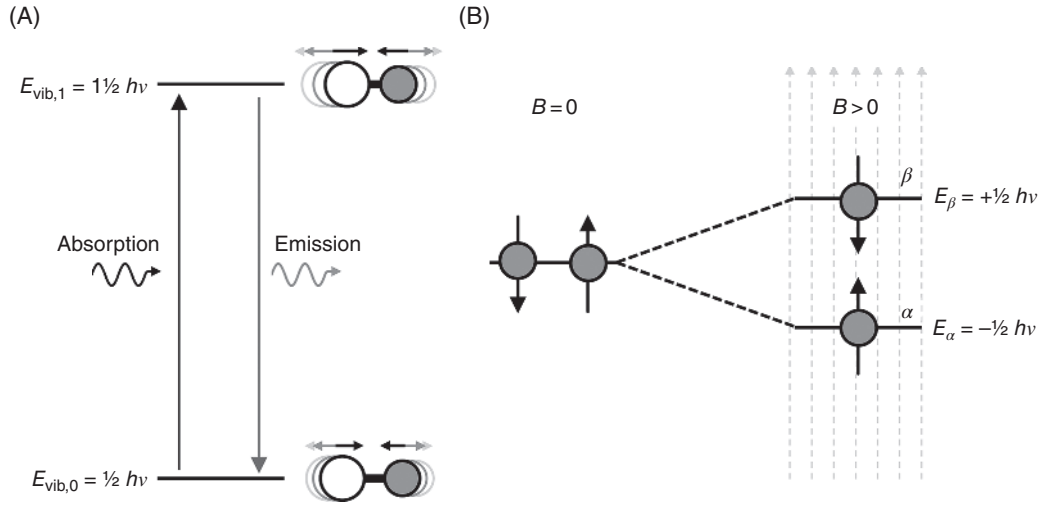

Figure 1.13 Quantum-mechanical view of spectroscopy. (A) A diatomic molecule can vibrate at different, but quantized frequencies. The energy levels associated with quantized vibrational modes can be investigated through the absorption or emission of electromagnetic radiation with a frequency that exactly matches the energy-level difference (i.e. $\nu = \Delta E/h$). Transitions in vibrational modes require frequencies in the infrared (IR) region of the electromagnetic spectrum (10^{12}–10^{14} Hz), hence giving rise to IR spectroscopy. (B) Quantum-mechanical view of NMR. In the absence of an external magnetic field ($B = 0$), the spin states are degenerate and no energy-level difference exists. In the presence of an external magnetic field ($B > 0$), the antiparallel (β) spin state is quantized at a higher energy level than the parallel (α) spin state. In analogy with IR spectroscopy in (A), the energy-level difference ΔE can be studied with electromagnetic waves of specific frequencies that match ΔE. For NMR, the frequencies are in the radiofrequency (RF) part of the electromagnetic spectrum (10^6–10^9 Hz).

energy level through the *emission* of electromagnetic waves of specific frequency ν. The IR spectrum of a compound contains unique frequencies related to the various vibrational modes allowed within its structure. IR spectroscopy is routinely used as an analytical tool for the identification of compounds or groups within compounds.

Intrinsic angular momentum, or spin, is also quantized both in amplitude and orientation. In the quantum mechanical picture of NMR spins are either in the parallel (α) or antiparallel (β) orientation with respect to the external magnetic field (Figure 1.13B). In the absence of an external magnetic field, the energy levels of the α and β spin-state are equal or degenerate. Application of an external magnetic field breaks the degeneracy, leading to different energy levels for the two spin orientations. This is referred to as the Zeeman effect, after Pieter Zeeman who in 1897 described the splitting of spectral lines of light in the presence of a magnetic field [52]. As shown in Figure 1.13B, the discrete energy levels associated with NMR are similar to that of any other quantum system (e.g. Figure 1.13A) and can thus be studied by spectroscopy. The spin states are characterized by energy $E = -mh\nu$ with m representing the spin quantum number associated with α ($m = ½$) and β ($m = -½$) spin orientations. Similar to IR spectroscopy (Figure 1.13A), NMR transitions are only allowed between energy levels for which the spin quantum number m changes by ±1 (Figure 1.13B). Emission is highly unlikely in NMR, as the energy levels are very close making the chance for spontaneous emission of a photon essentially zero. In the first observation of NMR by Purcell [1], the system was sampled by absorption of radiofrequency (RF) energy by protons in a strong magnetic field. Whereas both Bloch and Purcell detected the NMR phenomenon, their methodology and conceptualization were so different that it was not immediately obvious that they were observing the same effect.

In the quantum mechanical picture it may appear that all spins are either in the α or β spin state and that no other orientations are allowed. However, from earlier sections using classical arguments it is known that in a typical macroscopic sample most of the spins are in random orientations. The quantum mechanical view and the classical view can be reconciled to a certain degree by knowing that spins can, besides the pure α and β quantum states, also be in so-called superposition states. A superposition state is a spin state in which the pure or eigen α and β spin states are mixed and in which a spin can therefore attain any orientation. When an individual spin would be observed, as in the classical Stern–Gerlach experiment [53], the mixed or superposition state "collapses" into one of the pure α or β spin states. This forms one of the pillars of quantum mechanics. However, since NMR does not observe single spins, the collapse into pure spin states never happens and the spins within the sample remain in a superposition state throughout the experiment [35]. Since mixed states are simply a combination of the eigen or pure states, a quantum description of NMR typically uses the pure or eigen states to simplify the calculation.

In the case of noninteracting spins, like the protons in water, the quantum mechanical description of NMR presented in Figure 1.13 does not provide any additional insights. In fact it often causes confusion in the reconciliation between the spin-orientation sphere of Figures 1.2–1.4 and the pure α and β spin states of Figure 1.13. In the case of noninteracting spins it is therefore strongly advised to use the intuitive, classical description of NMR. However, in the case of interacting spins, as described in the next section, the classical picture will prove to be incomplete and the quantum description is required for a complete quantitative description.

1.12 Scalar Coupling

The NMR resonance frequencies, or chemical shifts, give direct information about the chemical environment of nuclei, thereby greatly aiding in the unambiguous detection and assignment of compounds. The integrated resonance area is, in principle (see Figure 1.8), directly proportional to the concentration of the compounds, thereby making NMR a quantitative technique. An additional feature that can be observed in NMR spectra is the splitting of resonances into several smaller lines, a phenomenon often referred to as scalar coupling, J coupling, or spin–spin coupling. Scalar coupling was first observed by Proctor and Yu [54] with $^{121}Sb/^{123}Sb$ NMR on an aqueous solution of $NaSbF_6$ and by Gutowsky and McCall [55] with ^{19}F and ^{31}P NMR on liquid phosphorus halides. Using the previously developed spin-echo method [56], Hahn and Maxwell [57] described scalar coupling as an additional modulation on the spin-echo envelope. Ramsey and Purcell [58] and Gutowsky et al. [59] subsequently provided a firm theoretical description.

Scalar coupling originates from the fact that nuclei with magnetic moments can influence each other, besides directly through space (dipolar coupling) also through electrons in chemical bonds (scalar coupling). Even though dipolar interactions are the main mechanism for relaxation in a liquid, there is no net interaction between nuclei since rapid molecular tumbling averages the dipolar interactions to zero. However, interactions through chemical bonds do not average to zero and give rise to the phenomenon of scalar coupling. Scalar coupling is a quantum effect that cannot be understood with the classical vector model alone. In Chapter 8 the classical description will be extended into a correlated vector model that can describe scalar coupling in a physically intuitive framework. For the remainder of this chapter scalar coupling will be explored within the quantum description of NMR.

Consider an isolated proton and an isolated carbon-13 atom as depicted in Figure 1.14A. Electrons in orbitals with an s character have a finite probability of being *inside* the nucleus, an example of a quantum effect without an exact classical analog. The Fermi contact governs the interaction between the nuclear and electron spins within the nucleus and energetically

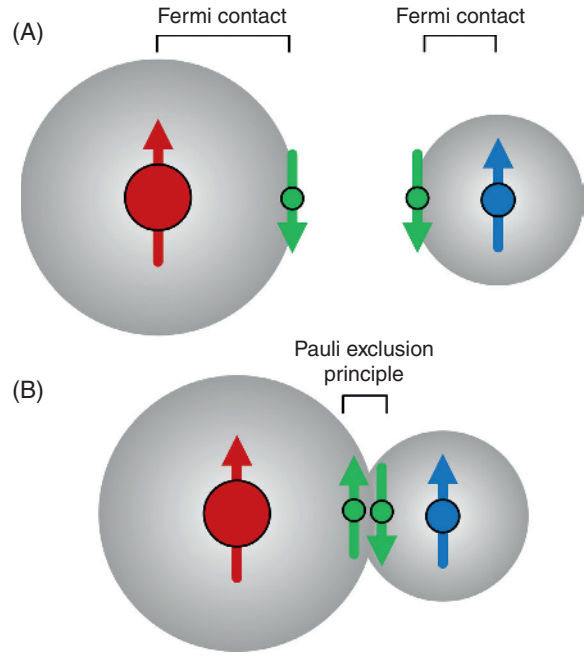

Figure 1.14 Nuclear and electron spin interactions. (A) In isolated atoms, the Fermi contact energetically favors an antiparallel orientation between nuclear and electronic spins. Proton, carbon-13 and electron spins are shown in blue, red and green respectively. (B) In chemical bonds, the Pauli exclusion principle demands that the electron spins are in an antiparallel orientation thereby potentially forcing nuclear and electron spins in an energetically higher parallel orientation, depending on the nuclear spin state.

favors an antiparallel over a parallel arrangement. In terms of energy-level diagrams, the ^{1}H and ^{13}C spins can be drawn as two separate, two-level diagrams (Figure 1.15A) or be combined into a single, four-level diagram (Figure 1.15B) with four energy levels, corresponding to the four nuclear spin combinations. In both cases, the energy level transitions in which the proton spin-orientation changes correspond to a resonance line at the proton frequency, whereas a spin flip for the ^{13}C nucleus corresponds to a resonance line in the ^{13}C NMR spectrum. The four allowed energy-level transitions (for which the spin quantum number m changes by ±1) give rise to two resonance frequencies, ν_H and ν_C, in agreement with the equivalent diagrams shown in Figure 1.15A.

Now consider the situation where the proton and carbon-13 nuclei are covalently bound, as for example in [1-^{13}C]-glucose (Figure 1.14B). The interaction between the two electrons inside a chemical bond is governed by the Pauli exclusion principle, which demands that the electron spins have an antiparallel orientation. When both nuclear spins are antiparallel to the external magnetic field B_0, i.e. the high-energy $\beta\beta$ state, the two bonding electrons cannot both be antiparallel to the nuclear spins, leading to an energetically less favorable state (Figure 1.15C). The $\beta\beta$ energy level increases by an amount proportional to $^{1}J_{CH}/4$ where $^{1}J_{CH}$ is the one-bond, heteronuclear scalar coupling constant expressed in Hz. Similar arguments can be used to describe the energy increase for the $\alpha\alpha$ state. However, for the $\alpha\beta$ and $\beta\alpha$ states both electron spins can be antiparallel to the nuclear spins leading to an energetically more favorable situation and a drop in energy level by an amount $^{1}J_{HC}/4$. In other words, an antiparallel orientation of the two nuclear spins is preferred for scalar coupling over a single bond. The energy level diagram for a scalar coupled two-spin-system still only allows four transitions, but they now correspond to four different frequencies at $\nu_H + {}^{1}J_{CH}/2$ and $\nu_H - {}^{1}J_{CH}/2$ on the proton channel and at $\nu_C + {}^{1}J_{CH}/2$ and $\nu_C - {}^{1}J_{CH}/2$ on the carbon-13 channel. Each of the resonances has been divided into two new resonances of equal intensity separated by $^{1}J_{CH}$, giving rise to the NMR spectrum shown in Figure 1.16.

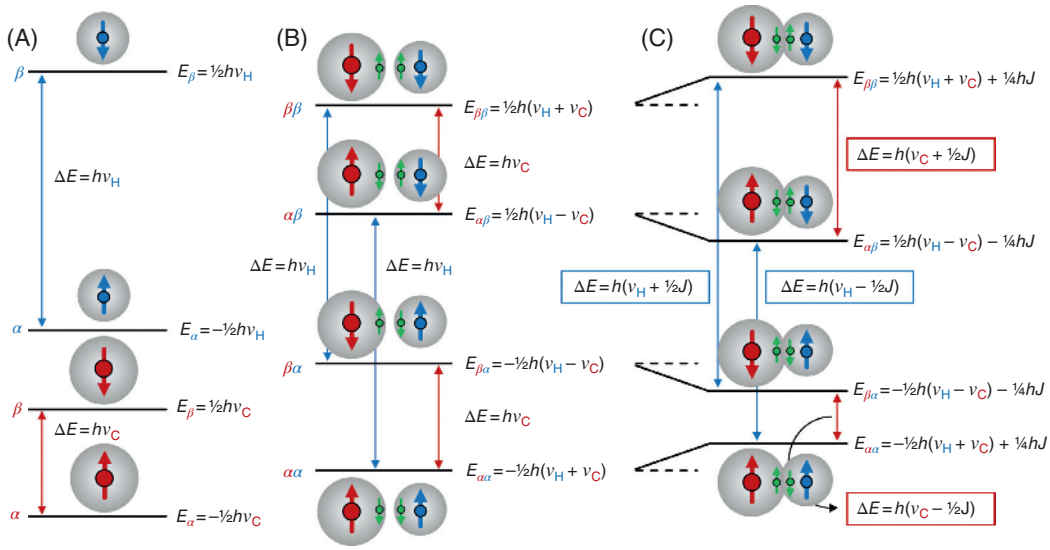

Figure 1.15 The effect of scalar coupling on the energy levels of a two-spin-system. (A) Energy-level diagram for isolated carbon-13 (red) and hydrogen (blue) nuclear spins drawn (A) separately or (B) combined. In the combined mode the energy levels simply represent the sum of the respective proton and carbon-13 energy levels. In both cases the blue and red energy-level differences correspond to proton and carbon-13 transitions of frequencies ν_H and ν_C, respectively. (C) Energy-level diagram for hydrogen and carbon-13 atoms attached via a chemical bond. The $\beta\beta$ spin state (i.e. the nuclear spin for both ^{13}C and ^{1}H is in the β state) becomes energetically less favorable as one of the two nuclear–electronic spin orientations is forced to be parallel (electron spins are shown in green). The same is true for the $\alpha\alpha$ spin-state, whereas in the $\alpha\beta$ and $\beta\alpha$ spin-states all spin orientations can be antiparallel. The shift in energy levels results in different frequencies for the proton ($\nu_H \pm J/2$) and carbon-13 ($\nu_C \pm J/2$) transitions. In other words, the single frequency ^{1}H and ^{13}C resonances in the absence of scalar coupling (B) are split into two resonances of half intensity, separated by the J coupling constant in the presence of scalar coupling (C) (see also Figure 1.16).

Similar arguments can be used to explain scalar coupling over two or three chemical bonds. In that case Hund's rule comes into play which states that the orbitals of a subshell are occupied with single electrons of parallel orientation before double occupation occurs. In the case of a sp^3 hybridization of the orbitals around a carbon nucleus, the electrons occupying each of the four orbital lobes are all in a parallel configuration. This fact, together with the Fermi contact interaction and the Pauli exclusion principle, make it that the $\alpha\alpha$ and $\beta\beta$ spin states between two protons attached to the carbon nucleus become the energetically favorable condition, moving down by an amount $^{1}J_{CH}/4$ (which is equivalent to moving up by an amount $-^{1}J_{CH}/4$). In other words, the sign of the scalar coupling constant becomes negative for scalar coupling over two bonds during which the parallel orientation between the nuclear spins becomes preferable. Using similar arguments it can be shown that the scalar coupling constant over three bonds becomes positive, whereby an antiparallel orientation between the two nuclear spins takes preference. The scalar coupling constant rapidly decreases with increasing number of chemical bonds and can typically be ignored for four or more bonds. The scalar coupling constant is independent of the applied external magnetic field, since it is based on the fundamental principle of spin–spin pairing and is therefore expressed in Hertz. Typical magnitudes of scalar coupling constants are, $^{1}H—^{1}H$ (1–15 Hz), $^{1}H—^{13}C$ (100–200 Hz), $^{1}H—^{15}N$ (70–110 Hz), $^{1}H—^{31}P$ (10–20 Hz), $^{13}C—^{13}C$ (30–80 Hz), and $^{31}P—O—^{31}P$ (15–20 Hz). All scalar coupling constants are for one chemical bond, except for $^{1}H—^{1}H$ and $^{31}P—O—^{31}P$ interactions which stretch over three and two bonds, respectively.

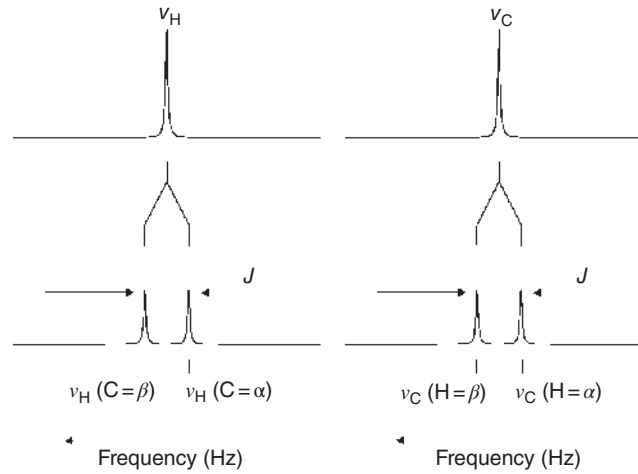

Figure 1.16 Resonance splitting due to scalar coupling. Scalar coupling between carbon-13 and hydrogen nuclei leads to a splitting of the singlet resonances into so-called doublet resonances. The resonances at the lower and higher frequencies are associated with energy-level transitions in which the nuclear spin of the scalar-coupling partner is in the α and β spin-state, respectively.

The spectrum shown in Figure 1.16 is only obtained when the frequency difference between the two scalar-coupled spins is much larger than the scalar coupling constant between them. For a heteronuclear interaction as shown in Figure 1.14 this requirement is certainly valid, as the frequency difference at magnetic fields commonly used for NMR is typically several tens of MHz, while the heteronuclear scalar coupling constant is less than 200 Hz. When the absolute frequency difference between two spins, $|\nu_1 - \nu_2|$, is much larger than their scalar coupling constant, J_{12}, the two spins form a weakly-coupled spin-system and the corresponding NMR spectrum is often referred to as a first-order spectrum. However, for many homonuclear interactions the frequency difference $|\nu_1 - \nu_2|$ is on the same order of magnitude as the homonuclear scalar coupling constant J_{12}, giving rise to so-called strongly-coupled spin-systems. In a strongly-coupled two-spin-system, the $\alpha\beta$ and $\beta\alpha$ spin-states become mixed such that a transition does no longer correspond to either spin 1 or 2 (as is the case in Figure 1.16), but contains contributions from both spins. As a result of this mixing of spin-states, the simple four-resonance-line spectrum (Figure 1.16) becomes more complicated as shown in Figure 1.17A. Strongly-coupled spin-systems produce so-called second-order spectra that are characterized by features not present in first-order spectra. Most noticeably from Figure 1.17A is the so-called "roof effect" in which a line from the outer to the inner resonances forms an imaginary roof. This effect is another feature of NMR spectra that indicates that two multiplets belong to the same molecule and can therefore aid in the identification of compounds. In the case of a two-spin-system, strong coupling only leads to a distortion of the resonance intensities and frequencies. However, for more complicated spin-systems strong coupling can lead to additional resonances (Figure 1.17B). Prime examples of strongly-coupled spin-systems *in vivo* are glutamate and glutamine.

It should be realized that while the behavior and spectral appearance of strongly-coupled spin-systems is no longer intuitive, it can still be quantitatively calculated through the use of the density matrix formalism, as will be discussed in Chapter 8. Note that the "roof effect" is also visible for more complicated spin-systems, as evident in Figure 1.17B.

1.13 Chemical and Magnetic Equivalence

The complexity of an NMR spectrum depends on the number of spins in different chemical environments within a chemical compound. Molecular symmetry can result in two or more spins having the exact same environment and hence having the same chemical shift. These

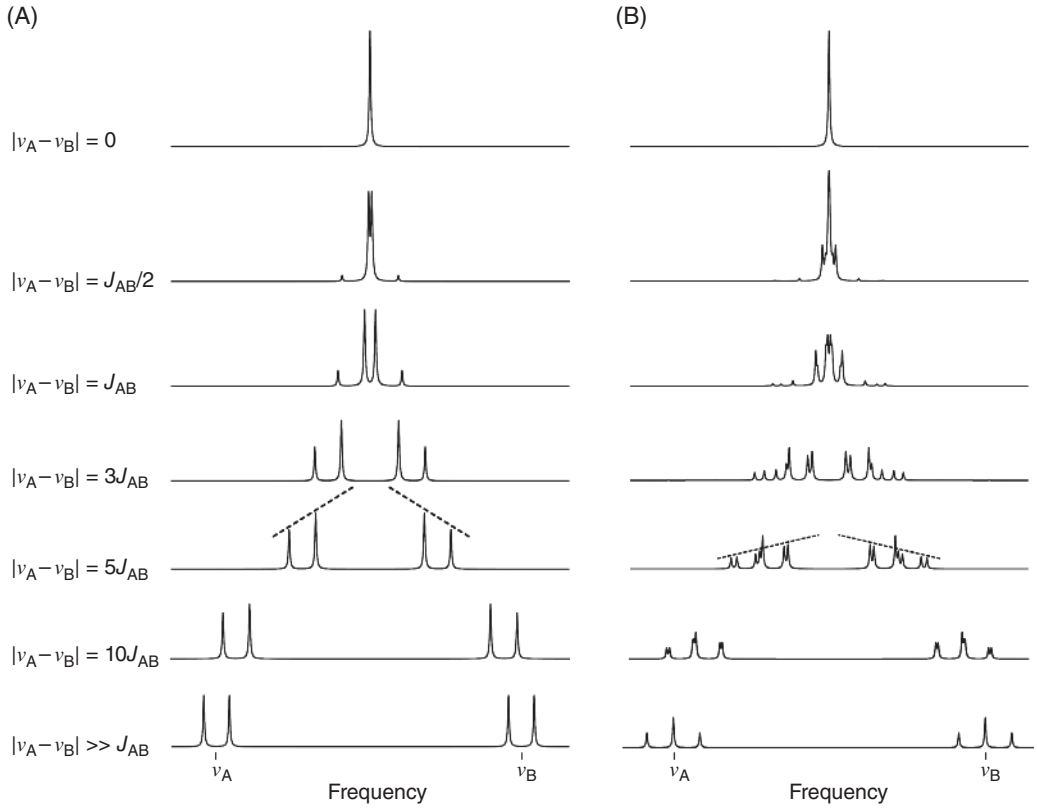

Figure 1.17 Spectral features for scalar-coupled spin-systems. Simulated (A) *AB* and (B) A_2B_2 NMR spectra showing the effects of varying the ratio of the scalar coupling constant to the frequency difference between the *A* and *B* resonances. The lower NMR spectra are indicative of weakly-coupled *AX* and A_2X_2 spin-systems, producing a first-order NMR spectrum, while the higher spectra are indicative of strongly-coupled *AB* and A_2B_2 spin-systems, displaying strong second-order effects, like the appearance of additional resonances, as well as the so-called "roof effect" (dotted lines). See text for details on spin-system nomenclature.

nuclei are said to be chemically equivalent. All physical and chemical properties, like reaction rates, exchange processes, and NMR chemical shift, are the same for chemically equivalent nuclei. Figure 1.18A and B shows an example of how a small chemical change can lead to a reduction in molecular symmetry and hence an increase in spectral complexity. *Scyllo*-inositol (Figure 1.18A) is characterized by six protons attached to a six-member carbon ring in which each proton is in a *trans* configuration relative to the adjacent protons. As a result, *scyllo*-inositol has a high degree of molecular symmetry making it that all six protons have identical chemical environments, leading to a single resonance line. *Myo*-inositol is an isomer of *scyllo*-inositol in which the proton on carbon position 2 is in a *cis* configuration with respect to its neighbors. This seemingly small change reduces the molecular symmetry of *myo*-inositol to a single plane. The remaining symmetry gives rise to four types of protons in four distinct chemical environments resulting in four NMR resonances (ignoring scalar coupling for the moment).

In order to understand the splitting pattern due to scalar coupling it is important to discriminate between magnetically equivalent and nonequivalent nuclei. Magnetic equivalence is a stronger version of chemical equivalence whereby nuclei have to satisfy an additional criterion; Nuclei are magnetically equivalent if they have identical scalar couplings with all other

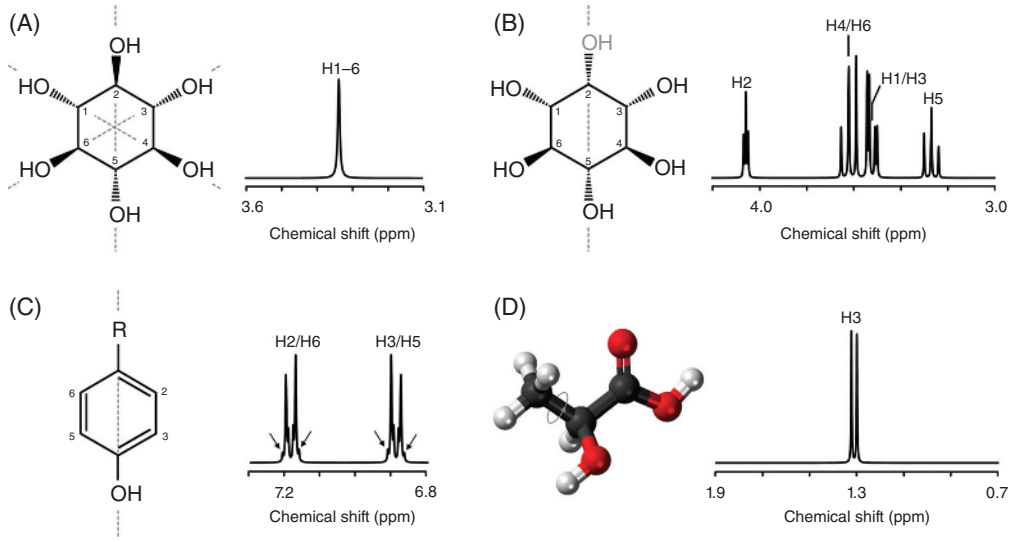

Figure 1.18 Chemical and magnetic equivalence. (A) Structure and ^{1}H NMR spectra of *scyllo*-inositol. The high degree of molecular symmetry makes all six protons chemically and magnetically equivalent, leading to the absence of scalar coupling. (B) Structure and ^{1}H NMR spectra of *myo*-inositol. The reduced molecular symmetry compared to *scyllo*-inositol leads to limited chemical equivalence and no magnetic equivalence. (C) Structure and ^{1}H NMR spectra of tyrosine, whereby R represents an alanine group. Protons 2/6 and 3/5 are chemical equivalent, but since the scalar coupling with other protons is not identical, they are not magnetically equivalent. Chemical equivalence without magnetic equivalence leads to a second-order ^{1}H NMR spectrum (arrows). (D) Structure and ^{1}H NMR spectra of lactate. Rapid rotation around the C2—C3 bond leads to chemical and magnetic equivalence of the three methyl protons, leading to a first-order ^{1}H NMR spectrum.

nonequivalent nuclei in the molecule. Magnetically equivalent nuclei do not produce an observable splitting among themselves, whereas magnetically nonequivalent (but chemically equivalent) nuclei always produce a second-order, strongly-coupled spectrum.

In *scyllo*-inositol (Figure 1.18A) all six protons are chemically equivalent and since there are no other nonequivalent nuclei in the molecule the six protons are also magnetically equivalent. This leads to a single resonance line without splitting due to scalar coupling. In *myo*-inositol (Fig. 1.18B), protons 1 and 3 are chemical equivalent. However, they are not magnetically equivalent since the scalar coupling with a nucleus outside the chemically equivalent group, e.g. proton 4, is not equal for protons 1 and 3 (i.e. $J_{14} = 0$ Hz and $J_{34} = 10$ Hz, making $J_{14} \neq J_{34}$). As a result, protons 1 and 3 *do* split among themselves due to scalar coupling. However, scalar coupling over four bonds in a non-aromatic ring is typically negligible and the splitting between protons 1 and 3 is not observed.

A similar situation arises in the aromatic ring of tyrosine (Figure 1.18C). Due to molecular symmetry protons 2 and 6 and protons 3 and 5 are chemically equivalent. However, since the scalar coupling between protons 2 and 3 and protons 6 and 3 are different, protons 2 and 6 are not magnetically equivalent. Since a four-bond coupling in an aromatic ring can often be readily detected, the NMR signal from protons 2 and 6 displays splitting due to scalar coupling which is automatically second-order since the chemical shifts are identical.

Chemical equivalence can also be achieved in the presence of rapid internal mobility. Consider the methyl protons of lactic acid (Figure 1.18D). The lack of molecular symmetry would suggest the absence of chemical equivalence. However, as the methyl group undergoes rapid rotation around the C2—C3 bond, each proton experiences a chemical environment that is averaged over all orientations. As the average chemical environment is identical for the three

protons, the protons in a methyl group are chemically equivalent. Since the coupling with the methine proton outside the methyl group is identical for all three protons, the methyl group is also magnetically equivalent.

A simple method of describing the effects of chemical and magnetic equivalence for any compound is provided by the Pople notation [60], after Nobel laureate John Pople. In the Pople notation, nuclei are indicated by letters, whereby the difference in chemical shift relative to the J-coupling constant is mirrored by the separation of the letters in the alphabet. Chemically equivalent nuclei are indicated by the same letter, whereby magnetically inequivalent nuclei are distinguished with a prime (e.g. A and A'). For the example shown in Figure 1.18, the Pople notations would be A_6 for *scyllo*-inositol and $AA'BB'MX$ for *myo*-inositol. Tyrosine is indicated as $AA'BB'$ and lactate as AX_3.

In the case of multiple, weakly-coupled spins the scalar coupling between each spin pair can be applied consecutively to arrive at the final splitting pattern. For example, in an AMX spin-system ($J_{AX} = 0$) the M spin couples with the A spin forming a doublet with scalar coupling J_{AM}. The M spin also couples with the X spin, such that each of the two M doublet lines splits again in two lines separated by J_{MX}, forming a final four-resonance, doublet-of-doublets signal. The presence of magnetically equivalent nuclei can lead to substantial simplification of the resulting NMR spectrum. If the aforementioned AMX spin-system is transformed to a MX_2 spin-system with two magnetically equivalent X spins, the final splitting pattern for the M spin would be composed of three signals; a doublet between M and X starts off the splitting pattern, after which each M signal is split again due to interaction with the second X spin. Since the two

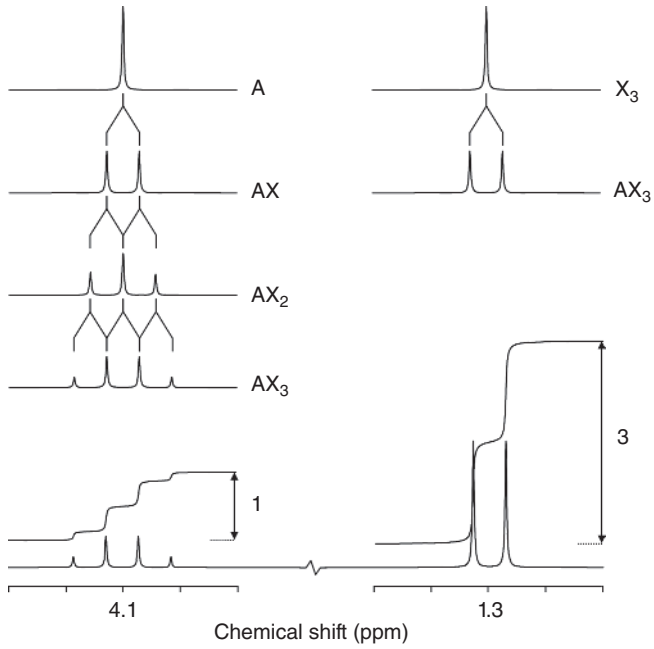

Figure 1.19 **^{1}H NMR spectrum of lactate.** The method of successive splitting for an AX_3 spin system (e.g. lactate, with a methyl group resonating at 1.31 ppm and a methine proton resonating at 4.10 ppm). The A resonance splits successively in a doublet, a triplet, and a quartet, while the X resonance splits into a doublet. Note that the binomial distribution (e.g. 1 : 3 : 3 : 1 for a quartet) only arises for magnetically equivalent nuclei which have an identical scalar coupling constant with a common coupling partner. Since the multiplet resonances at 4.10 and 1.31 ppm originate from one and three protons, respectively, the relative integrated areas of the two multiplets are therefore also one and three.

J-coupling constants are identical, the center peak gains double intensity resulting in a three-resonance, triplet signal with relative intensities of 1 : 2 : 1 among its resonances. The splitting pattern of spin A in an AX_n spin system (where n is the number of magnetically equivalent spins) is simply given by a binomial distribution in which the lines are separated by the scalar coupling constant (e.g. $n = 3$ results in a four-resonance quartet signal with amplitudes in a 1 : 3 : 3 : 1 ratio among its resonances).

Using these rules the appearance of all first-order spectra can be predicted. For example, Figure 1.19 shows the ^{1}H spectrum of lactic acid (lactate). Lactate can be seen as an AX_3 spin system, i.e. three magnetically equivalent methyl protons coupled to a nonequivalent single methine proton. Generally, the carbonyl and hydroxyl protons are invisible due to rapid exchange with water protons. Since the magnetically equivalent methyl protons do not produce any splitting among themselves, they only "feel" the methine proton, resulting in a doublet signal. The methine proton experiences three spins with an identical scalar coupling constant, resulting in four lines (a quartet) with a 1 : 3 : 3 : 1 binomial signal distribution. All the signals in the doublet and in the quartet are separated by the same scalar coupling constant. The relative integrated amplitude of the peaks at 1.31 and 4.10 ppm is 3 : 1, respectively, since there are three methyl protons versus one methine proton.

Exercises

1.1 A 2-l water-filled sphere ($T = 298.15$ K) is placed on a bench outside a 3.0 T MR magnet.

A Calculate the Larmor frequency of the proton spins outside the MR magnet (hint: Earth's magnetic field = 40 μT = 0.4 G).

B Calculate the Larmor frequency of the proton spins after the sphere is placed inside the MR magnet.

C For spins with a T_1 relaxation time constant of 4 s, calculate how much time is needed to reach 99% of the thermal equilibrium magnetization M_0 following placement of the water-filled sphere inside the MR magnet.

1.2 Derive the Bloch equations in the laboratory frame in the absence of relaxation (Eqs. (1.9)–(1.11)) from Eq. (1.8).

1.3 Show that free precession of the transverse magnetization according to

$$M_x(t) = M_x(0)\cos\omega t + M_y(0)\sin\omega t$$

and

$$M_y(t) = M_y(0)\cos\omega t - M_x(0)\sin\omega t$$

is a solution of the Bloch equations in the laboratory frame (Eqs. (1.9)–(1.11)) in the absence of a perturbing magnetic RF field.

1.4 **A** Derive the Bloch equations in the rotating frame (Eqs. (1.15)–(1.17)) from the Bloch equations in the laboratory frame (Eqs. (1.9)–(1.14)).

B Show that Eqs. (1.18) and (1.19) are solutions of the Bloch equations in the rotating frame (assume that $T_2 = T_2^*$).

1.5 **A** Derive the expression for the full line width at half maximum (FWHM) for the absorption component of a Lorentzian line (e.g. Eq. (1.23)).
B Derive the expression for the FWHM for the magnitude component of a Lorentzian line.
C Derive the expression for the absorption and dispersion parts of a resonance line originating from a full spin-echo (as opposed to an FID).
D Determine the peak heights and integrals of (the absorption component of) Lorentzian lines originating from an FID and a full spin-echo.

1.6 Longitudinal magnetization can be excited into the transverse plane by a 90° (or π/2) pulse.
A Starting from the Bloch equations in the rotating frame, derive an expression for the conversion of longitudinal magnetization M_z into transverse magnetization M_y by a RF pulse of length T and amplitude B_1 applied on-resonance along the x' axis. Show how the nutation angle depends on the pulse amplitude and length.
B If the pulse length of the 90° pulse is 1.0 ms, what is the required B_1 magnitude in μT to achieve excitation?
C How many Larmor precession cycles will occur in the laboratory frame at $B_0 = 3.0$ T during the 90° excitation pulse?

1.7 On a high-resolution NMR magnet (500 MHz for protons) signal is acquired as 16 384 points over a spectral width of 10 kHz. The sample consists of creatine in 99% D_2O and is acquired without water suppression. The magnetic field homogeneity is high, providing a spectral line width of 0.7 Hz for the creatine methyl signal. The relative peak heights of the creatine methylene (CH_2) and methyl (CH_3) signals are 1.2 and 3.0. Provide a likely explanation for the deviation from the expected 2 : 3 peak height ratio.

1.8 In a properly executed spin-echo sequence, the resonances of all (uncoupled) spins appear with the same relative phase. The absolute phase of all resonances can be made zero by a simple zero-order phase correction.
A Calculate the phase difference between the creatine methyl (3.03 ppm) and NAA methyl (2.01 ppm) proton resonances at 7.05 T in the presence of a 500 μs timing error.
B In a proton spectrum acquired at 3.0 T (water is on-resonance), the choline methyl (3.22 ppm) and NAA methyl (2.01 ppm) resonances appear with relative phases of 30° and 210°, respectively. Calculate the required zero- and first-order phase corrections to properly phase the spectrum to pure absorption lines.

1.9 Given the Gaussian line shape:

$$F_G(\omega) = \sqrt{\frac{\pi}{4}} M_0 T_{2G} e^{-(\omega_0-\omega)^2 T_{2G}^2/4}$$

A Find the expression for the full width at half maximum.
B For single Lorentzian and Gaussian resonance lines of equal line width and area, calculate the signal height-to-noise advantage of a Gaussian line (assuming equal noise levels).
C For single Lorentzian and Gaussian resonance lines of equal line width and area, calculate the line width advantage of a Gaussian line at 10% of the respective peak heights.

1.10 Consider a (hypothetical) ^{1}H NMR spectrum with the following five resonance:

Resonance 1: Triplet resonance ($^3J_{HH} = 7$ Hz) at 1.1 ppm with relative intensity (as determined by numerical integration) of 307.

Resonance 2: Quartet resonance ($^3J_{HH}$ = 7 Hz) at 3.9 ppm with relative intensity 198.
Resonance 3: Doublet-of-doublets ($^3J_{HH}$ = 11 and 8 Hz) at 7.2 ppm with relative intensity 102.
Resonance 4: Doublet resonance ($^3J_{HH}$ = 8 Hz) at 8.5 ppm with relative intensity 105.
Resonance 5: Doublet resonance ($^3J_{HH}$ = 11 Hz) at 10.0 ppm with relative intensity 96.

With the knowledge that the ^{1}H NMR spectrum originates from an organic molecule $C_5H_8O_2$, determine the complete chemical structure of the compound.

1.11 Consider a weakly-coupled four-spin-system AMX_2 with chemical shift positions given by δ_A = 5.0 ppm, δ_M = 1.5 ppm, and δ_X = 3.0 ppm.

A Sketch the NMR spectrum for this compound when J_{AM} = 20 Hz, J_{MX} = 10 Hz, and J_{AX} = 0 Hz. Assume equal T_1 and T_2 characteristics for all resonances.

B Sketch the NMR spectrum for this compound when J_{AM} = 20 Hz, J_{MX} = 10 Hz, and J_{AX} = 5 Hz. Assume equal T_1 and T_2 characteristics for all resonances.

C When the NMR spectrum is acquired with a pulse-acquire sequence (90° nutation angle, 500 ms repetition time TR, number of averages 8192) sketch the NMR spectrum for this compound when J_{AM} = 0 Hz, J_{MX} = 10 Hz, and J_{AX} = 0 Hz and T_{1A} = 5.0 s, T_{1M} = 1.0 s, and T_{1X} = 2.0 s. Assume equal T_2 characteristics for all resonances.

1.12 A proton NMR signal is acquired as 512 complex points during an acquisition time of 102.4 ms.

A Determine the spectral width of the experiment.

B Determine the apparent spectral frequency position of a signal with a frequency of +3800 Hz.

C Determine the apparent spectral frequency position of a signal with a frequency of −16 000 Hz.

1.13 In a proton NMR spectrum the resonance from DSS is detected at 170.345 213 MHz. Two other resonances occur at 170.345 453 and 170.354 668 MHz, respectively.

A Calculate the chemical shifts of the two resonances in ppm.

B Calculate the frequencies of the two compounds at 7.05 T when DSS appears at a frequency of 300.176 544 MHz.

1.14 The time-domain data from a sample consists of three sinusoidal functions (M_0 = 150, 300, 200) oscillating at different frequencies (250, 300, and 500 Hz) and decaying at different rates (T_2 = 50, 50, and 100 ms).

A Sketch the Fourier transform spectrum acquired from the sample when the initial phase is zero for all resonances. Indicate line widths (in Hz) and relative peaks heights.

B Sketch the Fourier transform spectrum acquired from the sample when the initial phases are 0°, 90°, and 135°, respectively.

1.15 Show that the real and imaginary frequency domain signals given by Eqs. (1.21) and (1.22) reduce to pure absorption and dispersion signals following a zero-order phase correction with $\phi_c = \phi$.

1.16 Hund's rule states that if two or more empty orbitals are available, electrons occupy each with spins parallel until all orbitals have one electron. When chemical bonds in sp^3 hybridized structures are considered, describe the signs of $^2J_{HH}$ and $^3J_{HH}$ relative to $^1J_{CH}$ using similar arguments as used for Figure 1.15.

References

1 Purcell, E.M., Torrey, H.C., and Pound, R.V. (1946). Resonance absorption by nuclear magnetic moments in a solid. *Phys. Rev.* 69: 37–38.
2 Bloch, F., Hansen, W.W., and Packard, M.E. (1946). Nuclear induction. *Phys. Rev.* 69: 127.
3 Bloch, F., Hansen, W.W., and Packard, M.E. (1946). The nuclear induction experiment. *Phys. Rev.* 70: 474–485.
4 Bloch, F. (1946). Nuclear induction. *Phys Rev* 70: 460–473.
5 Bloch, F. (1964). The principle of nuclear induction. In: *Nobel Lecturers in Physics 1942–1962*, 203–216. New York: Elsevier.
6 Purcell, E.M. (1964). Research in nuclear magnetism. In: *Nobel Lectures in Physics 1942–1962*, 219–231. New York: Elsevier.
7 Proctor, W.G. and Yu, F.C. (1950). The dependence of a nuclear magnetic resonance frequency upon chemical compound. *Phys. Rev.* 77: 717.
8 Dickinson, W.C. (1950). Dependence of the F19 nuclear resonance position on chemical compound. *Phys. Rev.* 77: 736.
9 Arnold, J.T., Dharmatti, S.S., and Packard, M.E. (1951). Chemical effects on nuclear induction signals from organic compounds. *J. Chem. Phys.* 19: 507.
10 Ernst, R.R. and Anderson, W.A. (1966). Applications of Fourier transform spectroscopy to magnetic resonance. *Rev. Sci. Instrum.* 37: 93–102.
11 Damadian, R. (1971). Tumor detection by nuclear magnetic resonance. *Science* 171: 1151–1153.
12 Moon, R.B. and Richards, J.H. (1973). Determination of intracellular pH by ^{31}P magnetic resonance. *J. Biol. Chem.* 248: 7276–7278.
13 Hoult, D.I., Busby, S.J., Gadian, D.G. et al. (1974). Observation of tissue metabolites using ^{31}P nuclear magnetic resonance. *Nature* 252: 285–287.
14 Behar, K.L., den Hollander, J.A., Stromski, M.E. et al. (1983). High-resolution ^{1}H nuclear magnetic resonance study of cerebral hypoxia *in vivo*. *Proc. Natl. Acad. Sci. U. S. A.* 80: 4945–4948.
15 Bottomley, P.A., Edelstein, W.A., Foster, T.H., and Adams, W.A. (1985). *In vivo* solvent-suppressed localized hydrogen nuclear magnetic resonance spectroscopy: a window to metabolism? *Proc. Natl. Acad. Sci. U. S. A.* 82: 2148–2152.
16 Aue, W.P., Bartholdi, E., and Ernst, R.R. (1976). Two-dimensional spectroscopy. Application to nuclear magnetic resonance. *J. Chem. Phys.* 64: 2229–2246.
17 Jeener, J. (1971). Ampere Summer School. Basko Polje, Yugoslavia.
18 Ernst, R.R. (1997). Nuclear magnetic resonance fourier transform spectroscopy. In: *Nobel Lectures, Chemistry 1991–1995*, 12–57. Singapore: World Scientific Publishing.
19 Wuthrich, K. (2003). NMR studies of structure and function of biological macromolecules. In: *Les Prix Nobel 2002*, 235–267. Sweden: Almquist and Wiksell International.
20 Lauterbur, P.C. (1973). Image formation by induced local interactions: examples employing nuclear magnetic resonance. *Nature* 242: 190–191.
21 Mansfield, P. and Grannell, P.K. (1973). NMR "diffraction" in solids? *J. Phys. C: Solid State Phys.* 6: L422–L427.
22 Lauterbur, P.C. (2004). All science is interdisciplinary – from magnetic moments to molecules to men. In: *The Nobel Prizes 2003*, 245–251. Stockholm: Nobel Foundation.
23 Mansfield, P. (2004). Snap-shot MRI. In: *The Nobel Prizes 2003*, 266–283. Stockholm: Nobel Foundation.
24 Haacke, E.M., Brown, R.W., Thompson, M.R., and Venkatesan, R. (1999). *Magnetic Resonance Imaging. Physical Principles and Sequence Design*. New York: Wiley-Liss.

25 Stark, D.D. and Bradley, W.G. (1999). *Magnetic Resonance Imaging*. New York: C. V. Mosby.
26 Bernstein, M.A., King, K.F., and Zhou, X.J. (2004). *Handbook of MRI Pulse Sequences*. Amsterdam: Academic Press.
27 Rabi, I.I. (1937). Space quantization in a gyrating magnetic field. *Phys. Rev.* 51: 652–654.
28 Rabi, I.I., Zacharias, J.R., Millman, S., and Kusch, P. (1938). A new method of measuring nuclear magnetic moment. *Phys. Rev.* 63: 318.
29 Rigden, J.S. (1986). Quantum states and precession: the two discoveries of NMR. *Rev. Mod. Phys.* 58: 433–448.
30 Becker, E.D., Fisk, C.L., and Khetrapal, C.L. (2007). Development of NMR: from the early beginnings to the early 1990s. *eMagRes* doi: 10.1002/9780470034590.emrhp0001.
31 Olson, J.A., Nordell, K.J., Chesnik, M.A. et al. (2000). Simple and inexpensive classroom demonstrations of nuclear magnetic resonance and magnetic resonance imaging. *J. Chem. Ed.* 77: 882–889.
32 Dirac, P.A.M. (1928). The quantum theory of the electron. *Proc. Roy. Soc. A* 117: 610–624.
33 Lowry, D.F. (1994). Correlated vector model of multiple-spin systems. *Concepts Magn. Reson.* 6: 25–39.
34 Levitt, M.H. (2005). *Spin Dynamics. Basics of Nuclear Magnetic Resonance*. New York: Wiley.
35 Hanson, L.G. (2008). Is quantum mechanics necessary for understanding magnetic resonance? *Concepts Magn. Reson.* 32: 329–340.
36 Larmor, J. (1897). On the theory of the magnetic influence on spectra; and on the radiation from moving ions. *Philos. Mag.* 44: 503–512.
37 Gorter, C.J. (1936). Negative result of an attempt to detect nuclear magnetic spins. *Physica* 3: 995–998.
38 Gorter, C.J. and Broers, L.J.F. (1942). Negative result of an attempt to observe nuclear magnetic resonance in solids. *Physica* 9: 591–596.
39 Hoult, D.I. (1989). The magnetic resonance myth of radio waves. *Concepts Magn. Reson.* 1: 1–5.
40 Hoult, D.I. (2009). The origin and present status of the radio wave controversy in NMR. *Concepts Magn. Reson.* 34: 193–216.
41 Bloch, F. and Siegert, A. (1940). Magnetic resonance for nonrotating fields. *Phys. Rev.* 57: 522–527.
42 Torrey, H.C. (1956). Bloch equations with diffusion terms. *Phys. Rev.* 104: 563–565.
43 McConnell, H.M. (1958). Reaction rates by nuclear magnetic resonance. *J. Chem. Phys.* 28: 430–431.
44 Wishart, D.S., Bigam, C.G., Yao, J. et al. (1995). ^{1}H, ^{13}C and ^{15}N chemical shift referencing in biomolecular NMR. *J. Biol. NMR* 6: 135–140.
45 Harris, R.K., Becker, E.D., Cabral de Menezes, S.M. et al. (2002). NMR nomenclature: nuclear spin properties and conventions for chemical shifts. IUPAC recommendations 2001. *Magn. Reson. Chem.* 40: 489–505.
46 Nyquist, H. (1928). Certain topics in telegraph transmission theory. *Trans. IEEE* 47: 617–644.
47 Bracewell, R.M. (1965). *The Fourier Transform and Its Applications*. New York: McGraw-Hill.
48 Ernst, R.R. (1966). *Sensitivity Enhancement in Magnetic Resonance*, Advances in Magnetic Resonance, vol. 2. New York: Academic Press.
49 Traficante, D.D. (1991). Time averaging, does the noise really average towards zero? *Concepts Magn. Reson.* 3: 83–87.
50 Cooley, J.W. and Tukey, J.W. (1965). An algorithm for machine calculation of complex Fourier series. *Math. Comput.* 19: 297–301.
51 Ernst, R.R., Bodenhausen, G., and Wokaun, A. (1987). *Principles of Nuclear Magnetic Resonance in One and Two Dimensions*. Oxford: Clarendon Press.

52 Zeeman, P. (1897). The effect of magnetisation on the nature of light emitted by a substance. *Nature* 55: 347.
53 Gerlach, W. and Stern, O. (1922). Der experimentelle nachweis des magnetischen moments des silberatoms. *Z. Phys.* 8: 110–111.
54 Proctor, W.G. and Yu, F.C. (1951). On the nuclear magnetic moments of several stable isotopes. *Phys. Rev.* 81: 20–30.
55 Gutowsky, H.S. and McCall, D.W. (1951). Nuclear magnetic resonance fine structure in liquids. *Phys. Rev.* 82: 748–749.
56 Hahn, E.L. (1950). Spin echoes. *Phys. Rev.* 80: 580–594.
57 Hahn, E.L. and Maxwell, D.E. (1952). Spin echo measurements of nuclear spin coupling in molecules. *Phys. Rev.* 88: 1070–1086.
58 Ramsey, N.F. and Purcell, E.M. (1952). Interactions between nuclear spins in molecules. *Phys. Rev.* 85: 143–144.
59 Gutowsky, H.S., McCall, D.W., and Slichter, C.P. (1953). Nuclear magnetic resonance multiplets in liquids. *J. Chem. Phys.* 21: 279–292.
60 Bernstein, H.J., Pople, J.A., and Schneider, W.G. (1957). The analysis of nuclear magnetic resonance spectra. *Can. J. Chem.* 35: 65–81.